

Thermomagnetic Ettingshausen-Nernst effect in tachocline and axion mechanism of solar luminosity variations

V.D. Rusov,¹ I.V. Sharph, V.P. Smolyar, M.E. Beglaryan

*Department of Theoretical and Experimental Nuclear Physics,
Odessa National Polytechnic University, Odessa, Ukraine*

M.V. Eingorn

*CREST and NASA Research Centers, North Carolina Central University,
Durham, North Carolina, U.S.A.*

ABSTRACT

It is shown that the hypothesis of the axion mechanism for solar luminosity variations suggesting that the solar axion particles are born in the core of the Sun and may be efficiently converted back into γ -quanta in the magnetic field of the solar overshoot tachocline is physically relevant. As a result, it is also shown that the intensity variations of the γ -quanta of axion origin, induced by the magnetic field variations in the tachocline via the thermomagnetic Ettingshausen-Nernst effect, directly cause the Sun luminosity variations and eventually characterize the active and quiet states of the Sun.

Within the framework of this mechanism estimations of the strength of the axion coupling to a photon ($g_{a\gamma} = 4.4 \cdot 10^{-11} \text{GeV}^{-1}$) and the hadronic axion particle mass ($m_a \sim 3.2 \cdot 10^{-2} \text{eV}$) have been obtained. It is also shown that the claimed axion parameters do not contradict any known experimental and theoretical model-independent limitations.

1. Introduction

A hypothetical pseudoscalar particle called axion is predicted by the theory related to solving the CP-invariance violation problem in QCD. The most important parameter determining the axion properties is the energy scale f_a of the so-called U(1) Peccei-Quinn symmetry violation. It determines both the axion mass and the strength of its coupling to fermions and gauge bosons including photons. However, in spite of the numerous direct experiments, they have not been discovered so far. Meanwhile, these experiments together with the astrophysical and cosmological limitations leave a rather narrow band for the permissible parameters of invisible axion (e.g. $10^{-6} \text{eV} \leq m_a \leq 10^{-2} \text{eV}$ (Raffelt 2004, 2008)), which is also a well-motivated cold dark matter candidate in this mass region (Raffelt 2004, 2008).

¹Corresponding author e-mail: siiis@te.net.ua

A whole family of axion-like particles (ALP) with their own features may exist along with axions having the similar Lagrangian structure relative to the Peccei-Quinn axion, as well as their own distinctive features. It consists in the fact that if they exist, the connection between their mass and their constant of coupling to photons must be highly weakened, as opposed to the axions. It should be also mentioned that the phenomenon of photon-ALP mixing in the presence of the electromagnetic field not only leads to the classic neutrino-like photon-ALP oscillations, but also causes the change in the polarization state of the photons (the $a\gamma\gamma$ coupling acts like a polarimeter (De Angelis et al. 2011)) propagating in the strong enough magnetic fields. It is generally assumed that there are light ALPs coupled only to two photons, although the realistic models of ALPs with couplings both to photons and to matter are not excluded (Masso 2008). Anyway, they may be considered a well-motivated cold dark matter candidate (Raffelt 2004, 2008) under certain conditions, just like axions.

It is interesting to note that the photon-ALP mixing in magnetic fields of different astrophysical objects including active galaxies, clusters of galaxies, intergalactic space and the Milky Way, may be the cause of the remarkable phenomena like dimming of stars luminosity (e.g. supernovae in the extragalactic magnetic field (Csaki et al. 2002; Mirizzi et al. 2005)) and “light shining through a wall” (e.g. light from very distant objects, travelling through the Universe (De Angelis et al. 2011; Fairbairn et al. 2011)). In the former case the luminosity of an astrophysical object is dimmed because some part of photons transforms into axions in the object’s magnetic field. In the latter case photons produced by the object are initially converted into axions in the object’s magnetic field, and then after passing some distance (the width of the “wall”) are converted back into photons in another magnetic field (e.g. in the Milky Way), thus emulating the process of effective free path growth for the photons in astrophysical medium (Adler et al. 2008; Redondo & Ringwald 2010).

For the sake of simplicity let us hereinafter refer to all such particles as axions if not stated otherwise.

In the present paper we consider the possible existence of the axion mechanism of Sun luminosity variations² based on the “light shining through a wall” effect. To be more exact, we attempt to explain the axion mechanism of Sun luminosity variations by the “light shining through a wall”, when the photons born mainly in the solar core are at first converted into axions via the Primakoff effect (Primakoff 1951) in its magnetic field, and then are converted back into photons after passing the solar radiative zone and getting into the magnetic field of the overshoot tachocline. We estimate this magnetic field within the framework of the Ettingshausen-Nernst effect. In addition to that we obtain the consistent estimates for the axion mass (m_a) and the axion coupling constant to photons ($g_{a\gamma}$), basing on this mechanism, and verify their values against the axion model results and the known experiments including CAST, ADMX, RBF.

²Let us point out that the axion mechanism of Sun luminosity used for estimating the axion mass was described for the first time in 1978 by Vysotskii et al. (1978).

2. Photon-axion conversion and the case of maximal mixing

Let us give some implications and extractions from the photon-axion oscillations theory which describes the process of the photon conversion into an axion and back under the constant magnetic field B of the length L . It is easy to show (Fairbairn et al. 2011; Raffelt & Stodolsky 1988; Mirizzi et al. 2005; Hochmuth & Sigl 2007) that in the case of the negligible photon absorption coefficient ($\Gamma_\gamma \rightarrow 0$) and axions decay rate ($\Gamma_a \rightarrow 0$) the conversion probability is

$$P_{a \rightarrow \gamma} = (\Delta_{a\gamma} L)^2 \sin^2 \left(\frac{\Delta_{osc} L}{2} \right) / \left(\frac{\Delta_{osc} L}{2} \right)^2, \quad (1)$$

where the oscillation wavenumber Δ_{osc} is given by

$$\Delta_{osc}^2 = (\Delta_{pl} + \Delta_{Q,\perp} - \Delta_a)^2 + 4\Delta_{a\gamma}^2 \quad (2)$$

while the mixing parameter $\Delta_{a\gamma}$, the axion-mass parameter Δ_a , the refraction parameter Δ_{pl} and the QED dispersion parameter $\Delta_{Q,\perp}$ may be represented by the following expressions:

$$\Delta_{a\gamma} = \frac{g_{a\gamma} B}{2} = 540 \left(\frac{g_{a\gamma}}{10^{-10} \text{GeV}^{-1}} \right) \left(\frac{B}{1G} \right) \text{ pc}^{-1}, \quad (3)$$

$$\Delta_a = \frac{m_a^2}{2E_a} = 7.8 \cdot 10^{-11} \left(\frac{m_a}{10^{-7} \text{eV}} \right)^2 \left(\frac{10^{19} \text{eV}}{E_a} \right) \text{ pc}^{-1}, \quad (4)$$

$$\Delta_{pl} = \frac{\omega_{pl}^2}{2E_a} = 1.1 \cdot 10^{-6} \left(\frac{n_e}{10^{11} \text{cm}^{-3}} \right) \left(\frac{10^{19} \text{eV}}{E_a} \right) \text{ pc}^{-1}, \quad (5)$$

$$\Delta_{Q,\perp} = \frac{m_{\gamma,\perp}^2}{2E_a}. \quad (6)$$

Here $g_{a\gamma}$ is the constant of axion coupling to photons; B is the transverse magnetic field; m_a and E_a are the axion mass and energy; $\omega_{pl}^2 = 4\pi\alpha n_e/m_e$ is an effective photon mass in terms of the plasma frequency if the process does not take place in vacuum, n_e is the electron density, α is the fine-structure constant, m_e is the electron mass; $m_{\gamma,\perp}^2$ is the effective mass square of the transverse photon which arises due to interaction with the external magnetic field.

The conversion probability (1) is energy-independent, when $2\Delta_{a\gamma} \approx \Delta_{osc}$, i.e.

$$P_{a \rightarrow \gamma} \cong \sin^2 (\Delta_{a\gamma} L), \quad (7)$$

or, whenever the oscillatory term in (1) is small ($\Delta_{osc} L/2 \rightarrow 0$), implying the limiting coherent behavior

$$P_{a \rightarrow \gamma} \cong \left(\frac{g_{a\gamma} B L}{2} \right)^2. \quad (8)$$

It is worth noting that the oscillation length corresponding to (7) reads

$$L_{osc} = \frac{\pi}{\Delta_{a\gamma}} = \frac{2\pi}{g_{a\gamma} B} \cong 5.8 \cdot 10^{-3} \left(\frac{10^{-10} \text{GeV}^{-1}}{g_{a\gamma}} \right) \left(\frac{1G}{B} \right) \text{ pc} \quad (9)$$

assuming a purely transverse field. In the case of the appropriate size L of the region a complete transition between photons and axions is possible.

From now on we are going to be interested in the energy-independent case (7) or (8) which plays the key role in determination of the parameters for the axion mechanism of Sun luminosity variations hypothesis (the axion coupling constant to photons $g_{a\gamma}$, the transverse magnetic field B of length L and the axion mass m_a).

3. Axion mechanism of Sun luminosity variations

Our hypothesis is that the solar axions which are born in the solar core (Raffelt 2004, 2008) through the known Primakoff effect (Primakoff 1951), may be converted back into γ -quanta in the magnetic field of the solar tachocline (the base of the solar convective zone). The magnetic field variations in the tachocline cause the converted γ -quanta intensity variations in this case, which in their turn cause the variations of the Sun luminosity known as the active and quiet Sun states. Let us consider this phenomenon in more detail below.

As we noted above, the expression (1) for the probability of the axion-photon oscillations in the transversal magnetic field was obtained for the media with the quasi-zero refraction, i.e. for the media with a negligible photon absorption coefficient ($\Gamma_\gamma \rightarrow 0$). It means that in order for the axion-photon oscillations to take place without any significant losses, a medium with a very low or quasi-zero density is required, which would suppress the processes of photon absorption almost entirely.

Surprisingly enough, it turns out that such “transparent” media can take place, and not only in plasmas in general, but straight in the convective zone of the Sun. Here we generally mean the so-called magnetic flux tubes, the properties of which are examined below.

3.1. Ideal photon channeling conditions inside the magnetic flux tubes

The idea of the energy flow channeling along a fanning magnetic field has been suggested for the first time by Hoyle (1949) as an explanation for darkness of umbra of sunspots. It was incorporated in a simple sunspot model by Chitre (1963). Zwaan (1978) extended this suggestion to smaller flux tubes to explain the dark pores and the bright faculae as well. Summarizing the research of the convective zone magnetic fields in the form of the isolated flux tubes, Spruit & Roberts (1983) suggested a simple mathematical model for the behavior of thin magnetic flux tubes, dealing with the nature of the solar cycle, sunspot structure, the origin of spicules and the source of mechanical heating in the solar atmosphere. In this model, the so-called thin tube approximation is used (see Spruit & Roberts (1983) and references therein), i.e. the field is conceived to exist in the form of slender bundles of field lines (flux tubes) embedded in a field-free fluid (Fig. 1). Mechanical

equilibrium between the tube and its surrounding is ensured by a reduction of the gas pressure inside the tube, which compensates the force exerted by the magnetic field. In our opinion, this is exactly the kind of mechanism [Parker \(1955b\)](#) was thinking about when he wrote about the problem of flux emergence: “Once the field has been amplified by the dynamo, it needs to be released into the convection zone by some mechanism, where it can be transported to the surface by magnetic buoyancy” ([Hassan 2003](#)).

In order to understand magnetic buoyancy, let us consider an isolated horizontal flux tube in pressure equilibrium with its non-magnetic surroundings so that in cgs units

$$p_{ext} = p_{int} + \frac{|\vec{B}|^2}{8\pi}, \quad (10)$$

where p_{int} and p_{ext} are the internal and external gas pressures respectively, B denotes the uniform field strength in the flux tube. If the internal and external temperatures are equal so that $T_{int} = T_{ext}$ (thermal equilibrium), then since $p_{ext} > p_{int}$, the gas in the tube is less dense than its surrounding ($\rho_{ext} > \rho_{int}$), implying that the tube will rise under the influence of gravity.

In spite of the obvious, though turned out to be surmountable, difficulties of the application to real problems, it was shown (see [Spruit & Roberts \(1983\)](#) and Refs. therein) that strong buoyancy forces act in magnetic flux tubes of the required field strength ($10^4 - 10^5$ G ([Ruzmaikin 2000](#))). Under their influence tubes either float to the surface as a whole (e.g. Fig. 1 in ([Fisher et al. 2000](#))) or they form loops of which the tops break through the surface (e.g. Fig. 1 in ([Zwaan 1978](#))) and lower parts descend to the bottom of the convective zone, i.e. to the overshoot tachocline zone. The convective zone, being unstable, enhanced this process ([Spruit & Van Ballegoijen 1982](#); [Golub et al. 1981](#)). Small tubes take longer to erupt through the surface because they feel stronger drag forces. It is interesting to note here that the phenomenon of the drag force which raises the magnetic flux tubes to the convective surface with the speeds about 0.3-0.6 km/s, was discovered in direct experiments using the method of time-distance helioseismology ([Ihonidis et al. 2011](#)). Detailed calculations of the process ([Moreno-Insertis 1982](#)) show that even a tube with the size of a very small spot, if located within the convective zone, will erupt in less than two years. Yet, according to [Moreno-Insertis \(1982\)](#), horizontal fields are needed in overshoot tachocline zone, which survive for about 11 yr, in order to produce an activity cycle.

A simplified scenario of magnetic flux tubes (MFT) birth and space-time evolution (Fig. 1a) may be presented as follows. MFT is born in the overshoot tachocline zone (Fig. 1c) and rises up to the convective zone surface (Fig. 1b) without separation from the tachocline (the anchoring effect), where it forms the sunspot (Fig. 1d) or other kinds of active solar regions when intersecting the photosphere. There are more fine details of MFT physics expounded in overviews by [Hassan \(2003\)](#) and [Fisher et al. \(2000\)](#), where certain fundamental questions, which need to be addressed to understand the basic nature of magnetic activity, are discussed in detail: How is the magnetic field generated, maintained and dispersed? What are its properties such as structure, strength, geometry? What are the dynamical processes associated with magnetic fields? **What role do magnetic fields play in energy transport?**

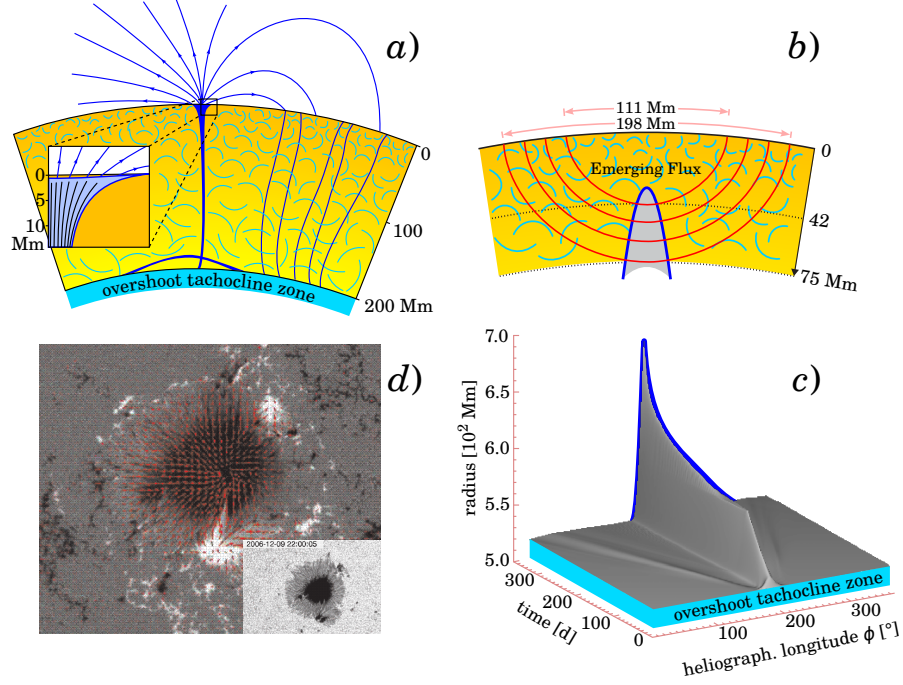


Fig. 1.— (a) Vertical cut through an active region illustrating the connection between a sunspot at the surface and its origins in the toroidal field layer at the base of the convection zone. Horizontal fields stored at the base of the convection zone (the overshoot tachocline zone) during the cycle. Active regions form from sections brought up by buoyancy (one shown in the process of rising). After eruption through the solar surface a nearly potential field is set up in the atmosphere (broken lines), connecting to the base of the convective zone via almost vertical flux tube. Hypothetical small scale structure of a sunspot is shown in the inset (Adopted from [Spruit \(2012\)](#) and [Spruit & Roberts \(1983\)](#)). (b) Detection of emerging sunspot regions in the solar interior ([Spruit 2012](#)). Acoustic ray paths with lower turning points between 42 and 75 Mm (1 Mm=1000 km) crossing a region of emerging flux. For simplicity, only four out of total of 31 ray paths used in this study (the time-distance helioseismology experiment) are shown here. Adopted from [Ilonidis et al. \(2011\)](#). (c) Emerging and anchoring of stable flux tubes in the overshoot tachocline zone, and its time-evolution in the convective zone. Adopted from [Caligari et al. \(1981\)](#). (d) Vector magnetogram of the white light image of a sunspot (taken with SOT on a board of the Hinode satellite – see inset) showing in red the direction of the magnetic field and its strength (length of the bar). The movie shows the evolution in the photospheric fields that has led to an X class flare in the lower part of the active region. Adopted from [Benz \(2008\)](#).

Dwelling on the last extremely important question associated with the energy transport, let us note that it is known that thin magnetic flux tubes can support longitudinal (also called sausage), transverse (also called kink), torsional (also called torsional Alfvén), and fluting modes (e.g. [Spruit \(1982\)](#); [Hollweg \(1990\)](#); [Roberts \(1991\)](#); [Roberts & Ulmschneider \(1997\)](#); [Stix \(2004\)](#)); for the tube modes supported by wide magnetic flux tubes, see [Roberts & Ulmschneider \(1997\)](#). Focusing on the longitudinal tube waves known to be an important heating agent of solar magnetic regions, it is necessary to mention the recent papers by [Fawzy et al. \(2012\)](#), which showed that the longitudinal flux tube waves are identified as insufficient to heat the solar transition region and corona in agreement with previous studies ([Fawzy & Cuntz 2011](#)). **In other words, the problem of generation and transport of energy by magnetic flux tubes remains unsolved in spite of its key role in physics of various types of solar active regions.**

It is clear that this unsolved problem of energy transport by magnetic flux tubes at the same time represents another unsolved problem related to the energy transport and sunspot darkness (see 2.2 in [Rempel & Schlichenmaier \(2011\)](#)). From a number of known concepts playing a noticeable role in understanding of the connection between the energy transport and sunspot darkness, let us consider the most significant theory, according to our vision. It is based on the Parker-Biermann cooling effect ([Parker 1955a](#); [Biermann 1941](#); [Parker 1979b](#)) and originates from the works of [Biermann \(1941\)](#) and [Alfvén \(1942\)](#).

The main point of the Parker-Biermann cooling effect is that the classical mechanism of the magnetic tubes buoyancy (e.g. Fig. 2a, [Parker \(1955a\)](#)), emerging as a result of the shear flows instability development in the tachocline, should be supplemented with the following results of the [Biermann \(1941\)](#) postulate and the theory developed by [Parker \(1955a, 1979b\)](#): the electric conductivity in the strongly ionized plasma may be so high that the magnetic field becomes frozen into plasma and causes the split magnetic tube (Fig. 2b,c) to cool inside.

Biermann understood that the magnetic field within the sunspots might itself be a reason of their darkness. Around the sunspots, the heat is transported up to the surface of the Sun by means of convection (see 2.2.1 in [Rempel & Schlichenmaier \(2011\)](#)), while [Biermann \(1941\)](#) noted that such transport is strongly inhibited by the nearly vertical magnetic field within the sunspot, thereby providing a direct explanation for the reduced temperature at the visible surface. Thus, the sunspot is dark because it is cooler than its surroundings, and it is cooler because the convection is inhibited underneath.

Still, the missing cause of a very high conductivity in strongly ionized plasma, which would produce a strong magnetic field “frozen” into this plasma, has been the major flaw of the so called [Biermann \(1941\)](#) postulate.

Let us show a solution to the known problem of the Parker-Biermann cooling effect, which is defined by the nature of the very large poloidal magnetic fields in the tachocline (determined by the thermomagnetic Ettingshausen-Nernst effect) and provides the physical basis for the photon channeling conditions inside the magnetic flux tubes.

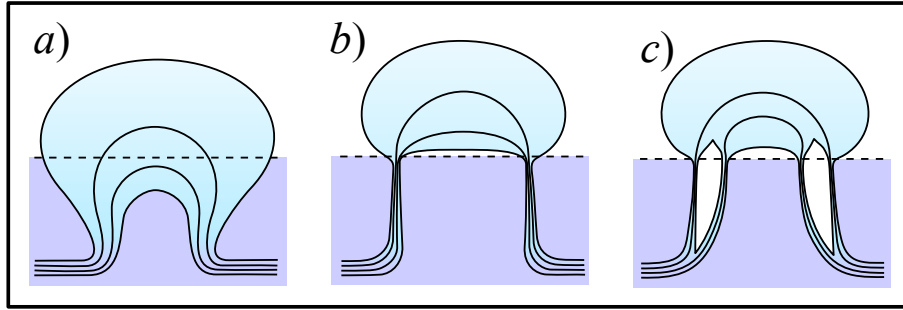


Fig. 2.— The possible ways of a toroidal magnetic flux tube development into a sunspot. (a) A rough representation of the form a tube can take after the rise to the surface by magnetic buoyancy (adopted from Fig. 2a in [Parker \(1955a\)](#)); (b) demonstrates the “crowding” below the photosphere surface because of cooling (adopted from Fig. 2b in [Parker \(1955a\)](#)); (c) demonstrates the tube splitting as a consequence of the inner region cooling under the conditions when the tube is in the thermal disequilibrium with its surroundings and the convective heat transfer is suppressed ([Biermann 1941](#)) above $\sim 0.71R_{Sun}$. This effect as well as the mechanism of the neutral atoms appearance inside the magnetic tubes are discussed further in the text (see Fig. 5a). Adopted from Fig. 2c in [Parker \(1955a\)](#).

3.1.1. The thermomagnetic Ettingshausen-Nernst effect and poloidal magnetic field in the tachocline

For the dynamo theories of planetary, stellar and spiral galactic magnetism the Coriolis force is of crucial importance. However, the assumed large solar dynamo leads to very large magnetic fields ($\sim 5 \cdot 10^7$ gauss ([Fowler et al. 1955](#); [Couvidat et al. 2003](#)), not observed on the surface of the Sun. This requires an explanation of how these fields are screened from reaching the surface.

As is known ([Schwarzschild 1958](#)), the temperature dependence of the thermonuclear reaction rate in the region of 10^7K goes in proportion to $T^{4.5}$. This means there is a sharp boundary between a much hotter region where most of the thermonuclear reactions occur and a cooler region where they are largely absent ([Winterberg 2015](#)). This boundary between radiative and convective zones is the tachocline. It is the thermomagnetic Ettingshausen-Nernst effect ([Ettingshausen & Nernst 1886](#); [Sondheimer 1948](#); [Spitzer 1956](#); [Kim & Stephen 1969](#)) which by the large temperature gradient in the tachocline between the hotter and cooler region leads to large currents shielding the large magnetic field of the dynamo ([Winterberg 2015](#)).

Subject to a quasi-steady state characterized by a balance of the magnetic field of the dynamo, in the limit of weak collision (the collision frequency much less than the cyclotron frequency of positive ions), a thermomagnetic current can be generated in a magnetized plasma ([Spitzer 1962, 2006](#)). For a fully ionized gases plasma the thermomagnetic Ettingshausen-Nernst effect leads to a current density given by (see Eqs. (5-49) in ([Spitzer 1962, 2006](#))):

$$\vec{j}_\perp = \frac{3kn_e c}{2B^2} \vec{B} \times \nabla T \quad (11)$$

where n_e is the electron number density, B is the magnetic field, and T is the absolute temperature (K). With $n_e = [Z/(Z+1)]n$, where $n = n_e + n_i$, and $n_i = n_e/Z$ is the ion number density for a Z -times ionized plasma, the following is obtained:

$$\vec{j}_\perp = \frac{3knc}{2B^2} \frac{Z}{Z+1} \vec{B} \times \nabla T. \quad (12)$$

It exerts a force on plasma, with the force density F given by

$$\vec{F} = \frac{1}{c} \vec{j}_\perp \times \vec{B} = \frac{3nk}{2B^2} \frac{Z}{Z+1} (\vec{B} \times \nabla T) \times \vec{B} \quad (13)$$

or with ∇T perpendicular to \vec{B}

$$\vec{F} = \frac{3nk}{2} \frac{Z}{Z+1} \nabla T \quad (14)$$

leading to the magnetic equilibrium condition (see Eqs. (4-1) in (Spitzer 1962))

$$\vec{F} = \frac{1}{c} \vec{j}_\perp \times \vec{B} = \nabla p \quad (15)$$

with $p = (\rho/m)kT = nkT$. And by equating (14) and (15),

$$\frac{3nk}{2} \frac{Z}{Z+1} \nabla T = nk \nabla T + kT \nabla n \quad (16)$$

or

$$a \frac{\nabla T}{T} + \frac{\nabla n}{n} = 0, \quad \text{where } a = \frac{2-Z}{2(Z+1)}, \quad (17)$$

we obtain the condition:

$$T^a n = \text{const.} \quad (18)$$

For a singly-ionized plasma with $Z = 1$, one has

$$T^{1/4} n = \text{const.} \quad (19)$$

For a doubly-ionized plasma ($Z = 2$) one has $n = \text{const.}$ Finally, in the limit $Z \rightarrow A$, one has $T^{-1/2} n = \text{const.}$ Therefore, n does not strongly depend on T , unlike in a plasma of constant pressure, in which $Tn = \text{const.}$ It shows that the thermomagnetic currents may change the pressure distribution in magnetized plasma considerably.

Taking a Cartesian coordinate system with z directed along ∇T , the magnetic field in the x -direction and the Ettingshausen-Nernst current in the y -direction, and supposing a fully ionized hydrogen plasma with $Z = 1$ in the tachocline, one has

$$j_\perp = j_y = -\frac{3nkc}{4B} \frac{dT}{dz}. \quad (20)$$

From Maxwell's equation $4\pi\vec{j}_\perp/c = \text{curl}\vec{B}$, one has

$$j_y = \frac{c}{4\pi} \frac{dB}{dz}, \quad (21)$$

and thus by equating (20) and (21) we obtain:

$$2B \frac{dB}{dz} = -6\pi k n \frac{dT}{dz}. \quad (22)$$

From (19) one has

$$n = \frac{n_{OT} T_{OT}^{1/4}}{T^{1/4}}, \quad (23)$$

where the values $n = n_{OT}$ and $T = T_{OT}$ correspond to the overshoot tachocline. Inserting (23) into (22), one finds

$$dB^2 = -\frac{6\pi k n_{OT} T_{OT}^{1/4}}{T^{1/4}} dT, \quad (24)$$

and hence, as a result of integration in the limits $[B_{OT}, 0]$ in the left-hand side and $[0, T_{OT}]$ in the right-hand side,

$$\frac{B_{OT}^2}{8\pi} = n_{OT} k T_{OT} \quad (25)$$

which shows that the magnetic field of the thermomagnetic current in the overshoot tachocline neutralizes the magnetic field of the dynamo reaching the overshoot tachocline (see Fig. 3).

Hence, it is not hard to understand what forces compress the field into intense filaments, in opposition to the enormous magnetic pressure

$$\frac{B_{OT}^2}{8\pi} = p_{ext} \approx 6.5 \cdot 10^{13} \frac{erg}{cm^3} \text{ at } 0.7R_{Sun}, \quad (26)$$

where the gas pressure p_{ext} at the tachocline of the Sun ($\rho \approx 0.2 \text{ g} \cdot \text{cm}^{-3}$ and $T \approx 2.3 \cdot 10^6 \text{ K}$ (Bahcall & Pinsonneault 1992) at $0.7R_{Sun}$) gives rise to a poloidal magnetic field

$$B_{OT} \simeq 4100T. \quad (27)$$

According to (27), a magnetic flux tube anchored in tachocline (see Fig. 4) has a significant toroidal magnetic field ($\sim 4100 \text{ T}$), within a layer near the base of the convection zone, where $0.7R_{Sun}$ and $d \sim 0.05R_{Sun}$ are constants defining the mean position and thickness of the layer where the field is concentrated. Each of these anchored magnetic flux tubes forms a pair of sunspots on the surface of the Sun.

Let us now show the theoretical possibility of the sunspot activity correlation with the variations of the γ -quanta of axion origin, induced by the magnetic field variations in the overshoot tachocline.

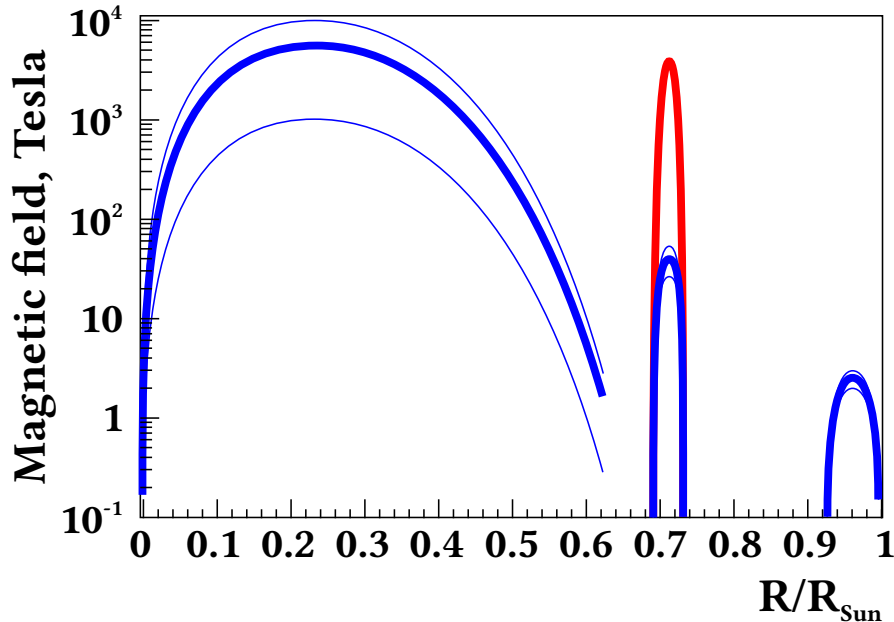


Fig. 3.— The reconstructed solar magnetic field (in blue) simulation from [Couvidat et al. \(2003\)](#): 10^3 - 10^4 Tesla (left), 30-50 Tesla (middle) and 2-3 Tesla (right), with a temperature of ~ 9 MK, ~ 2 MK and ~ 200 kK, respectively. The thin lines show the estimated range of values for each magnetic field component. Internal rotation was not included in the calculation. An additional axion production at those places can modify both intensity and shape of the solar axion spectrum (Courtesy Sylvaine Turck-Chièze (see Fig. 2 in [Zioutas et al. \(2007\)](#))). The reconstructed solar magnetic field (in red) simulation from [\(27\)](#): $4 \cdot 10^3$ T in tachocline ($\sim 0.7R_{Sun}$).

3.1.2. The Parker-Biermann cooling effect, Rosseland mean opacity and axion-photon oscillations in twisted magnetic tubes

Several local models are known to have been used with great success to investigate the formation of buoyant magnetic transport, which transforms twisted magnetic tubes generated through shear amplification near the base tachocline (e.g. [Nelson & Miesch \(2014\)](#)) and the structure and evolution of photospheric active regions (e.g. [Rempel \(2011\)](#)).

Because these models assume the anchored magnetic flux tubes depending on the poloidal field in the tachocline, it is not too hard to show that the magnetic field B_{OT} reaching $\sim 4100T$ (see [\(27\)](#)) may be at the same time the reason for the Parker-Biermann cooling effect in the twisted magnetic tubes (see Fig. 4b). The theoretical consequences of such reasoning of the Parker-Biermann cooling effect are considered below.

First of all, we suggest that the classic mechanism of magnetic tubes buoyancy (Fig. 4), appearing as a result of the shear instability development in the tachocline, should be supplemented

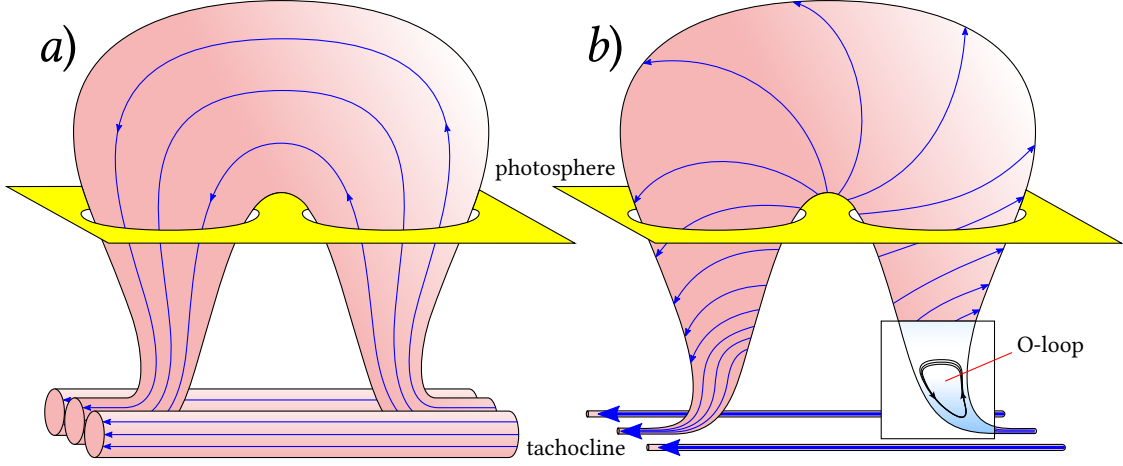


Fig. 4.— An isolated and anchored in tachocline (a) magnetic flux tube (adopted from Parker (1979a)) and (b) twisted magnetic flux tube (e.g. (Stein 2012), Fig. 2 in (Gold & Hoyle 1960), Fig. 1 and Fig. 2 in (Sturrock et al. 2001)) bursting through the solar photosphere to form a bipolar region. **Inset in panel (b):** topological effect of the magnetic reconnection in the magnetic tube (see Priest & Forbes (2000)), where the Ω -loop reconnects across its base, pinching off the Ω -loop to form a free O -loop (see Fig. 4 in Parker (1994)). The buoyancy of the O -loop is limited by the magnetic tube interior with Parker-Biermann cooling.

by the rise of the twisted magnetic tubes in a stratified medium (Fig. 4b (see Fig. 1 and Fig. 2 in (Sturrock et al. 2001))), where the magnetic field is produced by dynamo action throughout the convection zone, primarily by stretching and twisting in the turbulent downflows (see (Stein 2012)).

Second, the twisting of the magnetic tube may not only promote its splitting, but also may form a cool region under a certain condition

$$p_{ext} = \frac{B^2}{8\pi} \quad (28)$$

when the tube (inset in Fig. 4b) is in the thermal disequilibrium with its surroundings and the convective heat transfer is suppressed (Biermann 1941).

It is interesting to explore how the cool region stretching from the tachocline to the photosphere, where the magnetic tube is in thermal non-equilibrium (28) with its surroundings, deals with the appearance of the neutral atoms (e.g. hydrogen) in the upper convection zone (see Fig. 5a in contrast to Fig. 2c in Parker (1955b)). In other words, how does this very cool region prevent the neutral atoms to penetrate from the upper convection zone to the base of the convection zone, i.e. tachocline?

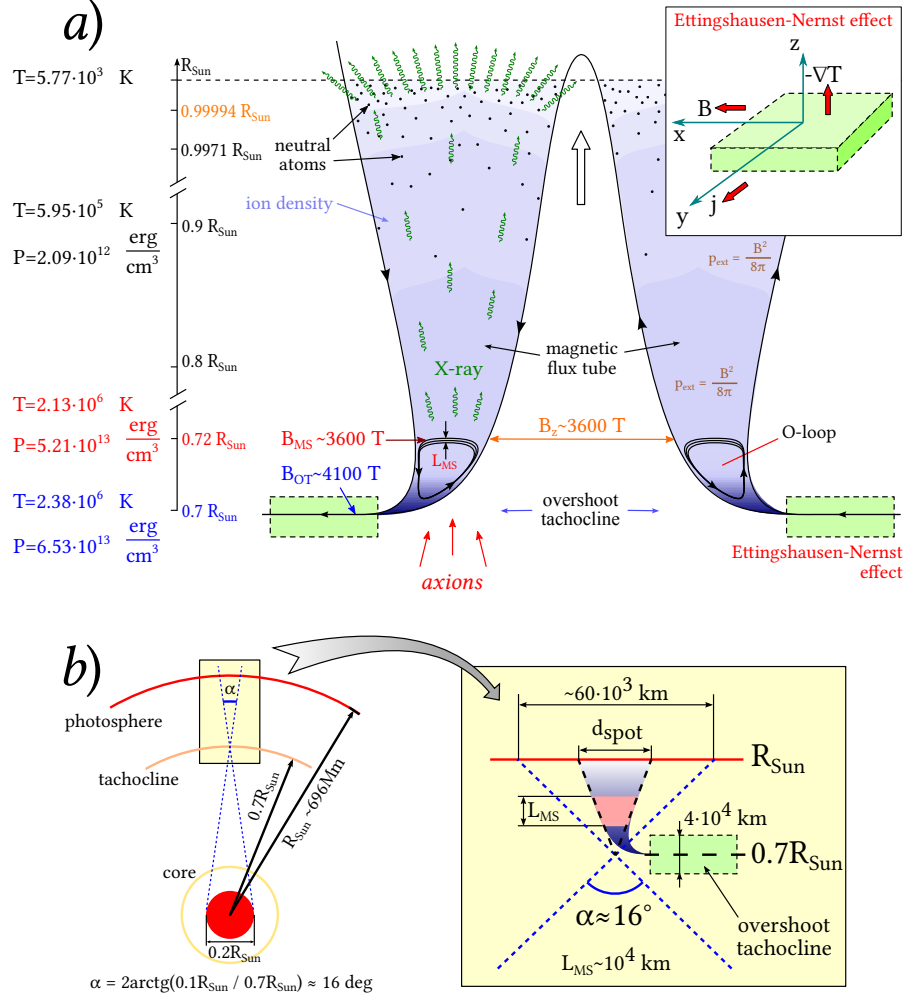


Fig. 5.— (a) Topological effects of the magnetic reconnection inside the magnetic tubes with the “magnetic steps”. The left panel shows the temperature and pressure change along the radius of the Sun from the tachocline to the photosphere (Bahcall & Pinsonneault 1992), L_{MS} is the height of the magnetic shear steps. At $R \sim 0.72 R_{\text{Sun}}$ the vertical magnetic field reaches $B_z \sim 3600 \text{ T}$, and the magnetic pressure $p_{\text{ext}} = B^2/8\pi \simeq 5.21 \cdot 10^{13} \text{ erg/cm}^3$ (Bahcall & Pinsonneault 1992). The very cool regions along the entire convective zone caused by the Parker-Biermann cooling effect have the magnetic pressure (28) in the twisted magnetic tubes.

(b) All the axion flux, born via the Primakoff effect (i.e. the real thermal photons interaction with the Coulomb field of the solar plasma) comes from the region $\leq 0.1 R_{\text{Sun}}$ (Zioutas et al. 2009). Using the angle $\alpha = 2 \arctan(0.1 R_{\text{Sun}}/0.7 R_{\text{Sun}})$ marking the angular size of this region relative to tachocline, it is possible to estimate the flux of the axions distributed over the surface of the Sun. The flux of the X-ray (of axion origin) is defined by the angle $\gamma = 2 \arctan(0.5 d_{\text{spot}}/0.3 R_{\text{Sun}})$, where d_{spot} is the diameter of a sunspot on the surface of the Sun (e.g. $d_{\text{spot}} \sim 11000 \text{ km}$ (Dikpati et al. 2008)).

It is essential to find the physical solution to the problem of solar convective zone which would fit the opacity experiments. The full calculation of solar opacities, which depend on the chemical composition, pressure and temperature of the gas, as well as the wavelength of the incident light, is a complex endeavour. The problem can be simplified by using a mean opacity averaged over all wavelengths, so that only the dependence on the gas physical properties remains (e.g. [Rogers & Iglesias \(1994\)](#); [Ferguson et al. \(2005\)](#); [Bailey et al. \(2009\)](#)). The most commonly used is the Rosseland mean opacity k_R , defined as:

$$\frac{1}{k_R} = \int_0^\infty d\nu \frac{1}{k_\nu} \frac{dB_\nu}{dT} \bigg/ \int_0^\infty d\nu \frac{dB_\nu}{dT} \quad (29)$$

where dB_ν/dT is the derivative of the Planck function with respect to temperature, k_ν is the monochromatic opacity at frequency ν of the incident light or the total extinction coefficient, including stimulated emission plus scattering. A large value of the opacity indicates strong absorption from beam of photons, whereas a small value indicates that the beam loses very little energy as it passes through the medium.

Note that the Rosseland opacity is an harmonic mean, in which the greatest contribution comes from the lowest values of opacity, weighted by a function that depends on the rate at which the blackbody spectrum varies with temperature (see Eq. (29) and Fig. 6), and the photons are most efficiently transported through the “windows” where k_ν is the lowest (see Fig.2 in [Bailey et al. \(2009\)](#)).

Taking the Rosseland mean opacities shown in Fig. 6, one may calculate, for example, four consecutive cool ranges within the convective zone (Fig. 5a), where the internal gas pressure p_{int} is defined by the following values:

$$p_{int} = nk_B T, \text{ where } \begin{cases} T \simeq 10^{3.48} \text{ K}, \\ T \simeq 10^{3.29} \text{ K}, \\ T \simeq 10^{3.20} \text{ K}, \\ T \simeq 10^{3.11} \text{ K}, \end{cases} \quad \rho = 10^{-7} \text{ g/cm}^3 \quad (30)$$

Since the inner gas pressure (30) grows towards the tachocline so that

$$\begin{aligned} p_{int}(T = 10^{3.48} \text{ K})|_{\leq 0.85R_{Sun}} &> p_{int}(T = 10^{3.29} \text{ K})|_{\leq 0.9971R_{Sun}} > \\ &> p_{int}(T = 10^{3.20} \text{ K})|_{\leq 0.99994R_{Sun}} > p_{int}(T = 10^{3.11} \text{ K})|_{\leq R_{Sun}}, \end{aligned} \quad (31)$$

it becomes evident that the neutral atoms appearing in the upper convection zone ($\geq 0.85R_{Sun}$) cannot descend deep to the base of the convection zone, i.e. tachocline (see Fig. 5a).

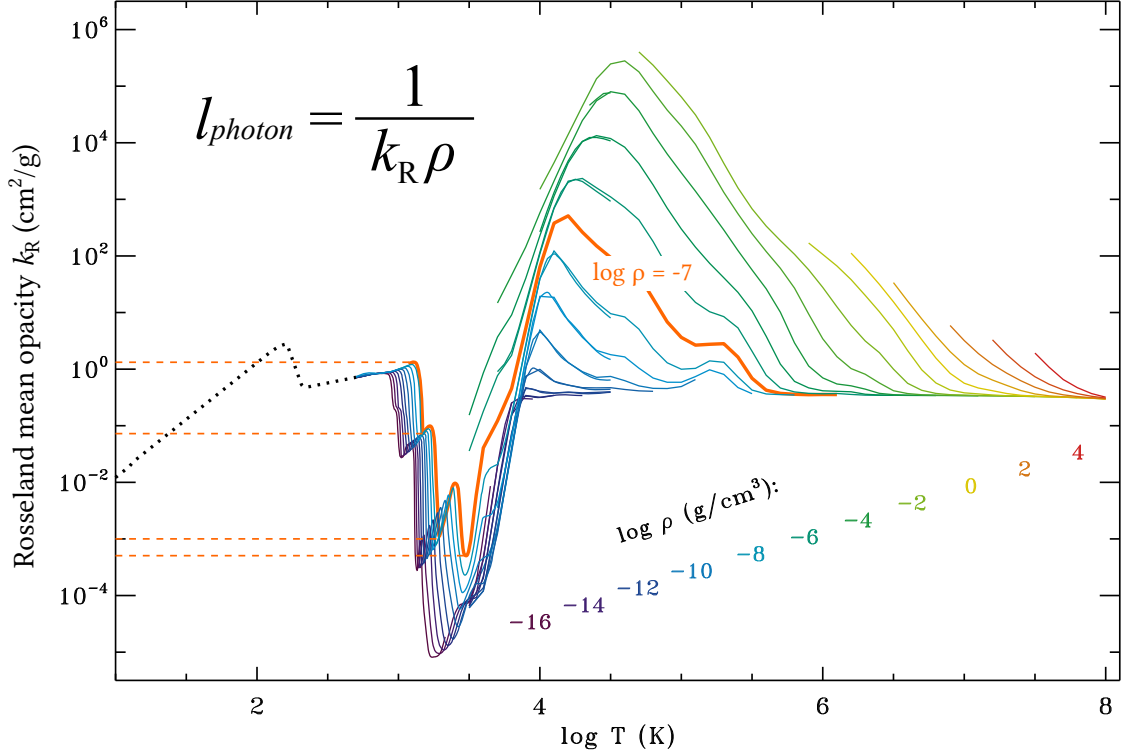


Fig. 6.— Rosseland mean opacity k_R , in units of cm^2g^{-1} , shown versus temperature (X-axis) and density (multi-color curves, plotted once per decade), computed with the solar metallicity of hydrogen and helium mixture $X=0.7$ and $Z=0.02$. The panel shows curves of k_R versus temperature for several “steady” values of the density, labelled by the value of $\log \rho$ (in g/cm^3). Curves that extend from $\log T = 3.5$ to 8 are from the Opacity Project (opacities.osc.edu). Overlapping curves from $\log T = 2.7$ to 4.5 are from [Ferguson et al. \(2005\)](#). The lowest-temperature region (black dotted curve) shows an estimate of ice-grain and metal-grain opacity from [D. Stamatellos et al. \(2007\)](#). Adapted from [Cranmer \(2015\)](#).

Therefore it is very important to examine the connection between the Rosseland mean opacity and axion-photon oscillations in twisted magnetic tube.

Let us consider the qualitative nature of the Ω -loop formation and growth process, based on the semiphenomenological model of the magnetic Ω -loops in the convective zone.

- A high concentration azimuthal magnetic flux ($B_{OT} \sim 4100$ T, see Fig. 5) in the overshoot tachocline through the shear flows instability development.

An interpretation of such link is related to the fact that helioseismology places the principal rotation $\partial\omega/\partial r$ of the Sun in the overshoot layer immediately below the bottom of the convective zone (Parker 1994). It is also generally believed that the azimuthal magnetic field of the Sun is produced by the shearing $r\partial\omega/\partial r$ of the poloidal field B_{OT} from which it is generally concluded that the principal azimuthal magnetic flux resides in the shear layer (Parker 1955b, 1993).

- If some “external” factor of the local shear perturbation appears against the background of the azimuthal magnetic flux concentration, such additional local density of the magnetic flux may lead to the magnetic field strength as high as, e.g. $B_z \sim 3600$ T (see Fig. 5a and Fig. 7b). Of course, this brings up a question about the physics behind such “external” factor and the local shear perturbation.

In this regard let us consider the superintense magnetic Ω -loop formation in the overshoot tachocline through the local shear caused by the high local concentration of the azimuthal magnetic flux. The buoyant force acting on the Ω -loop decreases slowly with concentration so the vertical magnetic field of the Ω -loop reaches $B_z \sim 3600$ T at about $R/R_{Sun} \sim 0.72$ (see Fig. 5a and Fig. 7b). Because of the magnetic pressure (see analog (26) and Fig. 5a) $p_{ext} = B_{0.72R_{Sun}}^2/8\pi = 5.21 \cdot 10^{13} \text{ erg/cm}^3$ (Bahcall & Pinsonneault 1992) this leads to a significant cooling of the Ω -loop tube (see Fig. 5a).

In other words, we assume the effect of the Ω -loop cooling to be the basic effect responsible for the magnetic flux concentration. It arises from the well known suppression of convective heat transport by a strong magnetic field (Biermann 1941). It means that although the principal azimuthal magnetic flux resides in the shear layer, it predetermines the additional local shear giving rise to a significant cooling inside the Ω -loop.

Thus, the ultralow pressure is set inside the magnetic tube as a result of the sharp limitation of the magnetic steps buoyancy inside the cool magnetic tube (Fig. 5a). This happens because the buoyancy of the magnetic flows requires finite **superadiabaticity** of the convection zone (Fan & Fisher 1996; Fan 2009), otherwise, expanding according to the magnetic **adiabatic** law (with the convection being suppressed by the magnetic field), the magnetic clusters may become cooler than their surroundings, which compensates the effect of the magnetic buoyancy of superintense magnetic O-loop.

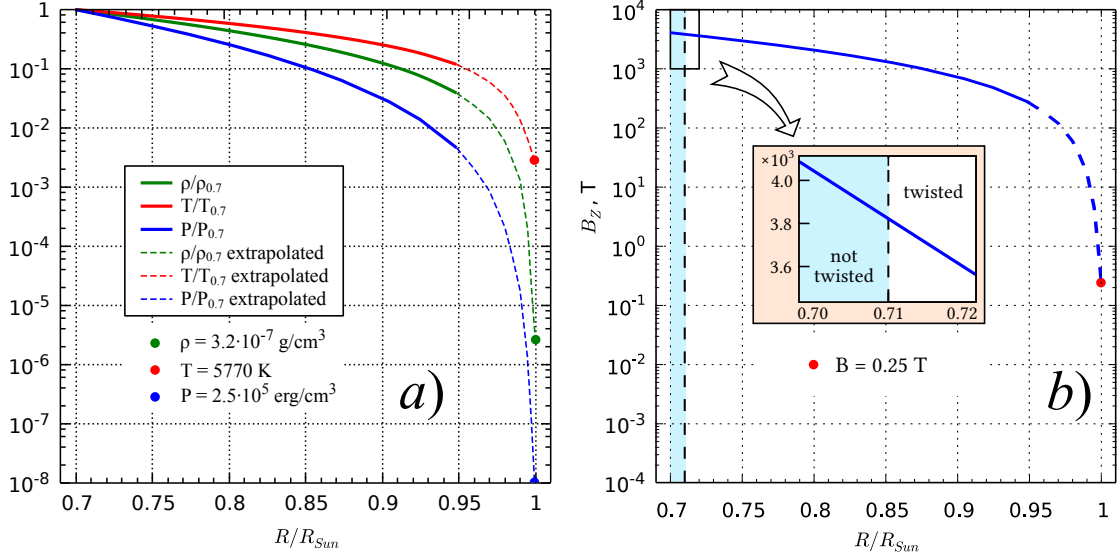


Fig. 7.— (a) Normalized external temperature, density and gas pressure as functions of the solar depth R/R_{Sun} . The standard solar model with He diffusion (Bahcall & Pinsonneault 1992) was used for $R < 0.95R_{Sun}$ (solid lines). The dotted lines mark extrapolated values. (b) Variation of the magnetic field strength B_z along the emerging Ω -loop as a function of the solar depth R/R_{Sun} throughout the convection zone. The solid blue line marks the permitted values for the same standard solar model with He diffusion (Bahcall & Pinsonneault 1992) starting at the theoretical estimate of the magnetic field $B_{OT} \approx B_z(0) = 4100 \text{ T}$. The dashed line is the continuation, according to the existence of the very cool regions inside the magnetic tube. Red point marks the up-to-date observations showing the mean magnetic field strength at the level $\sim 0.25 \text{ T} = 2500 \text{ G}$ (Pevtsov et al. 2011; Pevtsov et al. 2014).

Eventually we suppose that the axion mechanism based on the X-ray channeling along the “cool” region of the split magnetic tube (Fig. 5a) effectively supplies the necessary energy flux “channeling” in magnetic tube to the photosphere while the convective heat transfer is heavily suppressed.

In this context it is necessary to have a clear view of the energy transport by the X-ray of axion origin, which are a primary transfer mechanism. The recent improvements in the calculation of the radiative properties of solar matter have helped to resolve several long-standing discrepancies between observations and the predictions of theoretical models (e.g. Rogers & Iglesias (1994); Ferguson et al. (2005); Bailey et al. (2009)), and now it is possible to calculate the photon mean free path (Rosseland length) for Fig. 6:

$$l_{\text{photon}} = \frac{1}{k_R \rho} \sim \begin{cases} 2 \cdot 10^{10} \text{ cm} & \text{for } k_R \simeq 5 \cdot 10^{-4} \text{ cm}^2/\text{g}, \\ 10^{10} \text{ cm} & \text{for } k_R \simeq 10^{-3} \text{ cm}^2/\text{g}, \\ 1.5 \cdot 10^8 \text{ cm} & \text{for } k_R \simeq 6.7 \cdot 10^{-2} \text{ cm}^2/\text{g}, \\ 10^7 \text{ cm} & \text{for } k_R \simeq 1 \text{ cm}^2/\text{g}, \end{cases} \quad \rho = 10^{-7} \text{ g/cm}^3 \quad (32)$$

where the Rosseland mean opacity values k_R and density ρ are chosen so that the very low internal gas pressure p_{int} (see Eq. (31)) along the entire magnetic tube almost does not affect the external gas pressure p_{ext} (see (32) and Fig. 6).

Let us now examine the appearance of the X-ray of axion origin, induced by the magnetic field variations near the tachocline (Fig. 5a) and their impact on the Rosseland length (see (32)) inside the cool region of the magnetic tubes.

Let us remind that the magnetic field strength B_{OT} in the overshoot tachocline of $\sim 4100 \text{ T}$ (see Fig. 5a) and the Parker-Biermann cooling effect in (28) lead to the corresponding value of the magnetic field strength $B(z = 0.72R_{\text{Sun}}) \sim 3600 \text{ T}$ (see Fig. 5a), which in its turn assumes virtually zero internal gas pressure of the magnetic tube.

As it is shown above (see Priest & Forbes (2000)), the topological effect of the magnetic reconnection inside the Ω -loop results in the formation of the so-called O-loops (Fig. 4 and Fig. 5a) with their buoyancy limited from above by the strong cooling inside the Ω -loop (Fig. 5a). It is possible to derive the value of the horizontal magnetic field of the magnetic steps at the top of the O-loop: $|B_{MS}| \approx |B(z = 0.72R_{\text{Sun}})| \sim 3600 \text{ T}$.

So in the case of a large enough Rosseland length (see Eq. (32)), X-ray of axion origin induced by the horizontal magnetic field in O-loops, reach the photosphere freely, while in the photosphere itself, according to the Rosseland length

$$l_{\text{photon}} \approx 100 \text{ km} < l \approx 300 \div 400 \text{ km}, \quad (33)$$

these photons undergo a multiple Compton scattering (see Section 3.2) producing a typical directional pattern (Fig. 5a).

Aside from the X-rays of axion origin with mean energy of 4.2 keV , there are only $h\nu \sim 0.95 \text{ keV}$ X-rays (originating from the tachocline, according to a theoretical estimate by Bailey et al. (2009)) inside the magnetic tube. Such X-rays would produce the Compton-scattered photons with mean energy of $\leq 0.95 \text{ keV}$ which contradicts the known measurements of the photons with mean energy of $3\text{--}4 \text{ keV}$ (see Fig. 4 in Rieutord (2014)). Our suggested theoretical model thus removes these contradictions by involving the X-rays of axion origin *plus* the axions of the thermal X-ray origin, both produced in the magnetic field of O-loops (see Fig. 5a and Fig. B.1 in Appendix B).

And finally, let us emphasize that we have just shown a theoretical possibility of the time variation of the sunspot activity to correlate with the flux of the X-rays of axion origin; the latter being controlled by the magnetic field variations near the overshoot tachocline. As a result, it may be concluded that the axion mechanism for solar luminosity variations based on the lossless X-ray “channeling” along the magnetic tubes allows to explain the effect of the almost complete suppression of the convective heat transfer, and thus to understand the known puzzling darkness of the sunspots (Rempel & Schlichenmaier 2011).

3.2. Estimation of the solar axion-photon oscillation parameters on the basis of the hadron axion-photon coupling in white dwarf cooling

It is known (Cadamuro 2012) that astrophysics provides a very interesting clue concerning the evolution of white dwarf stars with their small mass predetermined by the relatively simple cooling process. It is related to the fact that recently it has been possible to determine their luminosity function with the unprecedented precision (Isern et al. 2008). It seems that if the DFSZ axion (Zhitnisky 1980; Dine et al. 1981) has a direct coupling to electrons and a decay constant $f_a \sim 10^9 \text{ GeV}$, it provides an additional energy-loss channel that permits to obtain a cooling rate that better fits the white dwarf luminosity function than the standard one (Isern et al. 2008). On the other hand, the KSVZ axion (Kim 1979; Shifman et al. 1980), i.e. the hadronic axion (with the mass in the meV range and $g_{a\gamma\gamma} \sim 10^{-12} \text{ GeV}^{-1}$) would also help in fitting the data, but in this case a stronger value for $g_{a\gamma\gamma}$ is required to perturbatively produce an electron coupling of the required strength (Cadamuro (2012), Fig. 1 in Srednicki (1985), Fig. 1 in Turner (1990), Eq. 82 in Kim & Carosi (2010)).

Our aim is to estimate the solar axion-photon oscillation parameters basing on the hadron axion-photon coupling derived from white dwarf cooling (see Appendix A). The estimate of the horizontal magnetic field in the O-loop is not related to the photon-axion conversion in the Sun only, but also to the axions in the model of white dwarf evolution. Therefore along with the values of the magnetic field strength $B_{MS} \sim 3600 \text{ T}$ and the height of the magnetic shear steps $L_{MS} \sim 1.28 \cdot 10^4 \text{ km}$ (Fig. 5a,b) we use the following parameters of the hadronic axion (from the White Dwarf area in Fig. 8a (Irastorza 2013; Carosi et al. 2013)):

$$g_{a\gamma} \sim 4.4 \cdot 10^{-11} \text{ GeV}^{-1}, \quad m_a \sim 3.2 \cdot 10^{-2} \text{ eV}. \quad (34)$$

The choice of these values is also related to the observed solar luminosity variations in the X-ray band (see (44)). The theoretical estimate and the consequences of such choice are considered below.

As it is shown above, the $\sim 4100 \text{ T}$ magnetic field in the overshoot tachocline and the Parker-Biermann cooling effect in (28) may produce the O-loops with the horizontal magnetic field of

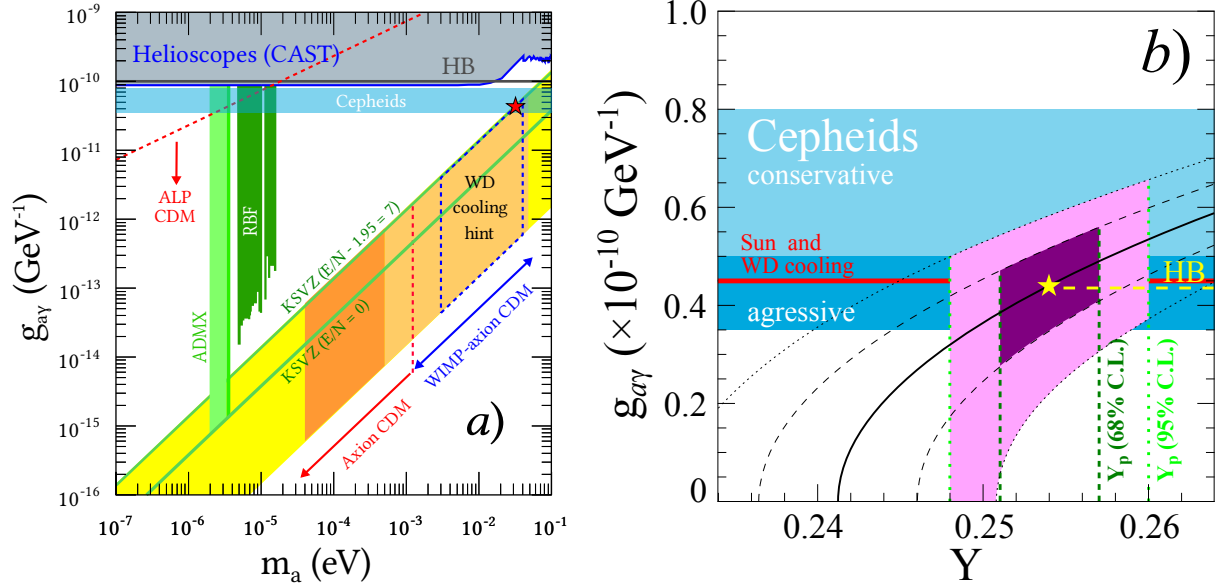


Fig. 8.— **(a)** Summary of astrophysical, cosmological and laboratory constraints on axions and axion-like particles. Comprehensive axion/ALP parameter space, highlighting the two main front lines of direct detection experiments: helioscopes (CAST (Andriamonje et al. 2007; Arik et al. 2009, 2011, 2013)) and haloscopes (ADMX (Asztalos et al. 2010) and RBF (Wuensch et al. 1989)). The astrophysical bounds from horizontal branch and massive stars are labeled “HB” (Raffelt 2008) and “Cepheids” (Carosi et al. 2013) respectively. The QCD motivated models (KSVZ (Kim 1979; Shifman et al. 1980) and DFSZ (Zhitnisky 1980; Dine et al. 1981)) for axions lay in the yellow diagonal band. The orange parts of the band correspond to cosmologically interesting axion models: models in the “classical axion window” possibly composing the totality of DM (labelled “Axiom CDM”) or a fraction of it (“WIMP-axion CDM” (Baer et al. 2011)). For more generic ALPs, practically all the allowed space up to the red dash line may contain valid ALP CDM models (Arias et al. 2012). The region of axion masses invoked in the WD cooling anomaly is shown by the blue dash line (Irastorza 2013). The red star marks the values of the axion mass $m_a \sim 3.2 \cdot 10^{-2} \text{ eV}$ and the axion-photon coupling constant $g_{a\gamma} \sim 4.4 \cdot 10^{-11} \text{ GeV}^{-1}$ chosen in the present paper on the basis of the suggested relation between the axion mechanisms of the Sun’s and the white dwarf luminosity variations.

(b) R parameter constraints to Y and $g_{a\gamma}$ (adopted from Ayala et al. (2014)). The dark purple area delimits the 68% C.L. for Y and R_{th} (see Eq. (1) in Ayala et al. (2014)). The resulting bound on the axion ($g_{10} = g_{a\gamma\gamma}/(10^{-10} \text{ GeV}^{-1})$) is somewhere between a rather conservative $0.5 < g_{10} \leq 0.8$ and most aggressive $0.35 < g_{10} \leq 0.5$ (Friedland et al. 2013). The red line marks the values of the axion-photon coupling constant $g_{a\gamma} \sim 4.4 \cdot 10^{-11} \text{ GeV}^{-1}$ chosen in the present paper. The blue shaded area represents the bounds from Cepheids observation. The yellow star corresponds to $Y=0.254$ and the bounds from HB lifetime (yellow dashed line).

$|B_{MS}| \approx |B(z = 0.72R_{Sun})| \sim 3600 \text{ T}$ stretching for about $L_{MS} \sim 1.28 \cdot 10^4 \text{ km}$, and surrounded by virtually zero internal gas pressure of the magnetic tube (see Fig. 5a).

It is not hard to use the expression (8) for the conversion probability³

$$P_{a \rightarrow \gamma} = \frac{1}{4} (g_{a\gamma} B_{MS} L_{MS})^2 \sim 1 \quad (35)$$

for estimating the axion coupling constant to photons (34).

Thus, it is shown that the hypothesis about the possibility for the solar axions born in the core of the Sun to be efficiently converted back into γ -quanta in the magnetic field of the magnetic steps of the O-loop (above the solar overshoot tachocline) is relevant. Here the variations of the magnetic field in the solar tachocline are the direct cause of the converted γ -quanta intensity variations. The latter in their turn may be the cause of the overall solar luminosity variations known as the active and quiet Sun phases.

It is easy to show that the theoretical estimate for the part of the axion luminosity L_a in the total luminosity of the Sun L_{Sun} with respect to (34) is (Andriamonje et al. 2007)

$$\frac{L_a}{L_{Sun}} = 1.85 \cdot 10^{-3} \left(\frac{g_{a\gamma}}{10^{-10} \text{ GeV}^{-1}} \right)^2 \sim 3.6 \cdot 10^{-4}. \quad (36)$$

As opposed to the classic mechanism of the Sun modulation, the axion mechanism is determined by the magnetic tubes rising to the photosphere, and not by the over-photosphere magnetic fields. In this case the solar luminosity modulation is determined by the axion-photon oscillations in the magnetic steps of the O-loop causing the formation and channeling of the γ -quanta inside the almost empty magnetic Ω -tubes (see Fig. 4 and Fig. 5a). When the magnetic tubes cross the photosphere, they “open” (Fig. 5a), and the γ -quanta are ejected to the photosphere, where their comfortable journey along the magnetic tubes (without absorption and scattering) ends. As the calculations by Zioutas et al. (2009) show, the further destiny of the γ -quanta in the photosphere may be described by the Compton scattering, which actually agrees with the observed solar spectral shape (Fig. 9b,c).

From the axion mechanism point of view it means that the solar spectra during the active and quiet phases (i.e. during the maximum and minimum solar activity) differ from each other by the smaller or larger part of the Compton spectrum, the latter being produced by the γ -quanta of the axion origin ejected from the magnetic tubes into the photosphere (see Fig. 4 in Chen et al. (2015)).

A natural question arises at this point: “What are the real parts of the Compton spectrum of the axion origin in the active and quiet phases of the Sun, and do they agree with the experiment?” Let us perform the mentioned estimations basing on the known experimental results

³Hereinafter we use rationalized natural units to convert the magnetic field units from *Tesla* to eV^2 , and the conversion reads $1 \text{ T} = 195 \text{ eV}^2$ (Guendelman et al. 2009).

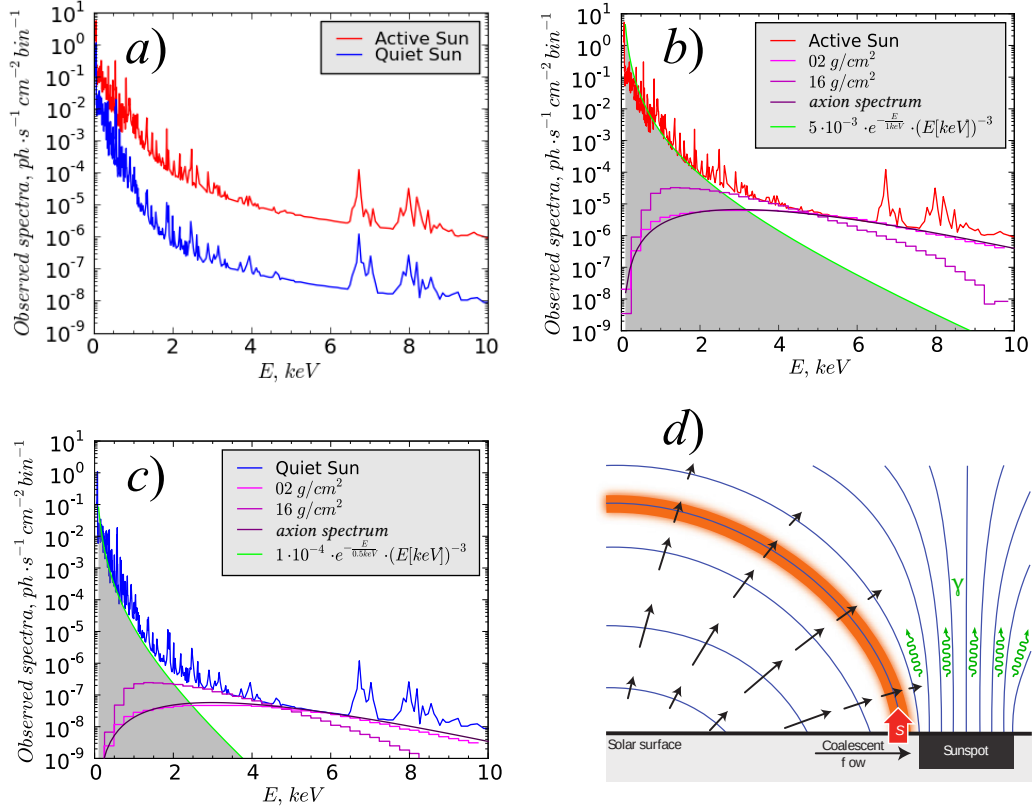


Fig. 9.— (a) Reconstructed solar photon spectrum below 10 keV from the active Sun (red line) and quiet Sun (blue line) from accumulated observations (spectral bin is 6.1 eV wide). Adopted from [Peres et al. \(2000\)](#).

(b) Reconstructed solar photon spectrum fit in the active phase of the Sun by the quasi-invariant soft part of the solar photon spectrum (grey shaded area; see Eq. (39)) and three spectra (42) degraded to the Compton scattering for column densities above the initial conversion place of 16 (adopted from [Zioutas et al. \(2009\)](#)) and 2 g/cm 2 (present paper).

(c) The similar curves for the quiet phase of the Sun (grey shaded area corresponds to Eq. (40))

(d) Cartoon showing the interplay between magnetic field expansion and the EUV loop. A coalescent flow forming the sunspot drags the magnetic field in the photosphere near the solar surface into the sunspot. In response, a hot spot of enhanced upward directed Poynting flux, S , forms (red arrow). The expanding field lines (blue) move upwards and to the side. When they transverse the hot spot of Poynting flux, the plasma on that field line gets heated and brightens up. As the field line expands further, it leaves the hot spot and gets darker again. In consequence a bright coronal EUV loop forms (orange) and remains rather stable as the successively heated field lines move through (adopted from [Chen et al. \(2015\)](#)). X-ray emission is the γ -quanta of axion origin coming from the magnetic tubes and not related to the magnetic reconnection as conjectured by e.g. [Shibata & Magara \(2011\)](#).

by ROSAT/PSPC, where the Sun’s coronal X-ray spectra and the total luminosity during the minimum and maximum of the solar coronal activity were obtained (Peres et al. 2000).

Apparently, the solar photon spectrum below 10 keV of the active and quiet Sun (Fig. 9a) reconstructed from the accumulated ROSAT/PSPC observations may be described by three Compton spectra for different column densities rather well (Fig. 9b,c). This gives grounds for the assumption that the hard part of the solar spectrum is mainly determined by the axion-photon conversion efficiency:

$$\left(\frac{d\Phi}{dE}\right)^{(*)} \simeq \left(\frac{d\Phi}{dE}\right)_{corona}^{(*)} + \left(\frac{d\Phi_{\gamma}}{dE}\right)_{axions}^{(*)}, \quad (37)$$

where $\frac{d\Phi}{dE}$ is the observed solar spectra during the active (red line in Fig. 9a,b) and quiet (blue line in Fig. 9a,c) phases, $\left(\frac{d\Phi}{dE}\right)_{corona}$ represents the power-like theoretical solar spectra

$$\left(\frac{d\Phi}{dE}\right)_{corona} \sim E^{-(1+\alpha)} e^{-E/E_0}, \quad (38)$$

where a power law decay with the “semi-heavy tail” takes place in practice (Lu et al. 1993) instead of the so-called power laws with heavy tails (Lu & Hamilton 1991; Lu et al. 1993) (see e.g. Figs. 3 and 6 in Uchaikin (2013)). Consequently, the observed corona spectra ($0.25 \text{ keV} < E \leq 2.5 \text{ keV}$) (shaded area in Fig. 9b)

$$\left(\frac{d\Phi}{dE}\right)_{corona}^{(active)} \sim 5 \cdot 10^{-3} \cdot (E [\text{keV}])^{-3} \cdot \exp\left(-\frac{E}{1 \text{ keV}}\right) \text{ for the active Sun} \quad (39)$$

and (shaded area in Fig. 9c)

$$\left(\frac{d\Phi}{dE}\right)_{corona}^{(quiet)} \sim 1 \cdot 10^{-4} \cdot (E [\text{keV}])^{-3} \cdot \exp\left(-\frac{E}{0.5 \text{ keV}}\right) \text{ for the quiet Sun}; \quad (40)$$

$\left(\frac{d\Phi_{\gamma}}{dE}\right)_{axions}$ is the reconstructed solar photon spectrum fit ($0 \text{ keV} < E < 10 \text{ keV}$) constructed from three spectra (42) degraded to the Compton scattering for different column densities (see Fig. 9b,c for the active and quiet phases of the Sun respectively).

As is known, this class of flare models (Eqs. (39) and (40)) is based on the recent paradigm in statistical physics known as self-organized criticality (Bak et al. 1987; Bak et al. 1988; Bak & Chen 1989; Bak 1996; Aschwanden 2011). The basic idea is that the flares are a result of an “avalanche” of small-scale magnetic reconnection events cascading (Lu et al. 1993; Charbonneau et al. 2001; Aschwanden 2014) through the highly intense coronal magnetic structure (Shibata & Magara 2011)

driven at the critical state by the accidental photospheric movements of its magnetic footprints. Such models thus provide a natural and computationally convenient basis for the study of Parker hypothesis of the coronal heating by nanoflares (Parker 1988).

Another significant fact discriminating the theory from practice, or rather giving a true understanding of the measurements against some theory, should be recalled here (e.g. (38) (see Eq. (5) in Lu et al. (1993))). The nature of power laws is related to the strong connection between the consequent events (this applies also to the “catastrophes”, which in turn gives rise to a spatial nonlocality related to the appropriate structure of the medium (see page 45 in Uchaikin (2013))). As a result, the “chain reaction”, i.e. the avalanche-like growth of perturbation with more and more resource involved, leads to the heavy-tailed distributions. On the other hand, obviously, none of the natural events may be characterized by the infinite values of mean and variance. Therefore, the power laws like (38) are approximate and must not hold for the very large arguments. It means that the power law decay of the probability density rather corresponds to the average asymptotics, and the “semi-heavy tails” must be observed in practice instead.

In this regard we suppose that the application of the power-law distributions with semi-heavy tails leads to a soft attenuation of the observed corona spectra (which are not visible above $E > 2 \div 3 \text{ keV}$), and thus to a close coincidence between the observed solar spectra and γ -spectra of axion origin (Fig. 9). I.e.

$$\left(\frac{d\Phi}{dE}\right)^{(*)} \simeq \left(\frac{d\Phi_\gamma}{dE}\right)^{(*)}_{axions} \quad \text{for energies } E > 2 \div 3 \text{ keV}. \quad (41)$$

It means that the physics of the formation and ejection of the γ -quanta above $2 \div 3 \text{ keV}$ through the sunspots into corona is not related to the magnetic reconnection theory by e.g. Shibata & Magara (2011) (Fig. 9d), and may be of the axion origin.

With this in mind, let us suppose that the part of the differential solar axion flux at the Earth (Andriamonje et al. 2007)

$$\frac{d\Phi_a}{dE} = 6.02 \cdot 10^{10} \left(\frac{g_{a\gamma}}{10^{10} \text{ GeV}^{-1}}\right)^2 E^{2.481} \exp\left(-\frac{E}{1.205}\right) \text{ cm}^{-2} \text{ s}^{-1} \text{ keV}^{-1}, \quad (42)$$

which characterizes the differential γ -spectrum of the axion origin $d\Phi_\gamma/dE$ (see $[d\Phi_\gamma/dE]_{axions}$ in (37) and (41))

$$\frac{d\Phi_\gamma}{dE} \cong P_\gamma \frac{d\Phi_a}{dE} \text{ cm}^{-2} \text{ s}^{-1} \text{ keV}^{-1} \approx 6.1 \cdot 10^{-3} P_\gamma \frac{d\Phi_a}{dE} \text{ ph} \cdot \text{cm}^{-2} \text{ s}^{-1} \text{ bin}^{-1} \quad (43)$$

where the spectral bin width is 6.1 eV (see Fig. 9a); the probability P_γ describing the relative portion of γ -quanta (of axion origin) channeling along the magnetic tubes may be defined, according to Peres et al. (2000), from the observed solar luminosity variations in the X-ray band,

recorded in ROSAT/PSPC experiments (Fig. 9): $(L_{corona}^X)_{min} \approx 2.7 \cdot 10^{26} \text{ erg/s}$ at minimum and $(L_{corona}^X)_{max} \approx 4.7 \cdot 10^{27} \text{ erg/s}$ at maximum,

$$P_\gamma = P_{a \rightarrow \gamma} \cdot \frac{\Omega \cdot (0.5d_{spot})^2}{(\tan(\alpha/2) \cdot 0.3R_{Sun})^2} \cdot \Lambda_a \approx 3.4 \cdot 10^{-3}, \quad (44)$$

directly following from the geometry of the system (Fig. 5b), where the conversion probability $P_{a \rightarrow \gamma} \sim 1$ (35);

$$\Omega = (I_\gamma \text{ CZ}/I_0) \cdot (I_\gamma \text{ photo}/I_\gamma \text{ CZ}) \cdot (I_\gamma \text{ corona}/I_\gamma \text{ photo}) \approx 0.23 \quad (45)$$

is the total relative intensity of γ -quanta, where $(I_\gamma \text{ CZ}/I_0) \sim 1$ is the relative intensity of γ -quanta “channeling” through the magnetic tubes in the convective zone, $I_\gamma \text{ photo}/I_\gamma \text{ CZ} = \exp[-(\mu l)_{photo}] \sim 0.23$ (see Eq. 54) is the relative intensity of the Compton-scattered γ -quanta in the solar photosphere, and $I_\gamma \text{ corona}/I_\gamma \text{ photo} = \exp[-(\mu l)_{corona}] \approx 1$ (see Eq. 55) is the relative intensity of the Compton-scattered γ -quanta in the solar corona; d_{spot} is the measured diameter of the sunspot (umbra) (Dikpati et al. 2008; Gough 2010). Its size determines the relative portion of the axions hitting the sunspot area. Further,

$$\frac{(0.5d_{spot})^2}{(\tan(\alpha/2) \cdot 0.3R_{Sun})^2} \cong 0.034, \quad (46)$$

where

$$0.5d_{spot} = \left[\frac{1}{\pi} \left(\frac{\langle \text{sunspot area} \rangle_{max}}{\langle N_{spot} \rangle_{max}} \right) \right]^{(1/2)} \cong 5500 \text{ km}, \quad (47)$$

and the value Λ_a characterizes the portion of the axion flux going through the total $(2 \langle N_{spot} \rangle_{max})$ sunspots on the photosphere:

$$\Lambda_a = \frac{(\text{sunspot axion flux})}{(1/3)(\text{total axion flux})} \approx \frac{2 \langle N_{spot} \rangle_{max} (\tan(\alpha/2) \cdot 0.3R_{Sun})^2}{(4/3)R_{Sun}^2} \sim 0.42, \quad (48)$$

and $\langle N_{spot} \rangle_{max} \approx 150$ is the average number of the maximal sunspot number, and $\langle \text{sunspot area} \rangle_{max} \approx 7.5 \cdot 10^9 \text{ km}^2 \approx 2470 \text{ ppm of visible hemisphere}$ is the sunspot area (over the visible hemisphere (Dikpati et al. 2008; Gough 2010)) for the cycle 22 experimentally observed by the Japanese X-ray telescope Yohkoh (1991) (Zioutas et al. 2009).

On the other hand, from the known observations (see Peres et al. (2000) and Appendix B)

$$\frac{(L_{corona}^X)_{max}}{L_{Sun}} \cong 1.22 \cdot 10^{-6}, \quad (49)$$

where $L_{Sun} = 3.8418 \cdot 10^{33} \text{ erg/s}$ is the solar luminosity (Bahcall & Pinsonneault 2004). Using the theoretical axion impact estimate (36), one can clearly see that the obtained value (44) is in good agreement with the observations (49):

$$P_\gamma = \frac{(L_{corona}^X)_{max}}{L_{Sun}} \bigg/ \frac{L_a}{L_{Sun}} \sim 3.4 \cdot 10^{-3}, \quad (50)$$

derived independently.

In other words, if the hadronic axions found in the Sun are the same particles found in the white dwarfs with the known strength of the axion coupling to photons (see (34) and Fig. 8a,b), it is quite natural that the independent observations give the same estimate of the probability P_γ (see (44) and (50)). So the consequences of the choice (34) are determined by the independent measurements of the average sunspot radius, the sunspot number (Dikpati et al. 2008; Gough 2010), the model estimates of the horizontal magnetic field and the height L_{MS} of the magnetic steps (see Fig. 5), and the hard part of the solar photon spectrum mainly determined by the axion-photon conversion efficiency, and the theoretical estimate for the part of the axion luminosity L_a in the total luminosity of the Sun L_{Sun} (50).

4. Axion mechanism of the solar Equator – Poles effect

The axion mechanism of Sun luminosity variations is largely validated by the experimental X-ray images of the Sun in the quiet (Fig. 10a) and active (Fig. 10b) phases (Zioutas et al. 2009) which clearly reveal the so-called Solar Equator – Poles effect (Fig. 10b).

The essence of this effect lies in the following. It is known that the axions may be transformed into γ -quanta by inverse Primakoff effect in the transverse magnetic field only. Therefore the axions that pass towards the poles (blue cones in Fig. 10b) and equator (the blue band in Fig. 10b) are not transformed into γ -quanta by inverse Primakoff effect, since the magnetic field vector is almost collinear to the axions' momentum vector. The observed nontrivial X-ray distribution in the active phase of the Sun may be easily and naturally described within the framework of the axion mechanism of the solar luminosity variations.

As described in Section 3.1, the photons of axion origin travel through the convective zone along the magnetic flux tubes, up to the photosphere. In the photosphere they are Compton-scattered, which results in a substantial deviation from the initial axions directions of propagation (Fig. 11).

Let us make a simple estimate of the Compton scattering efficiency in terms of the X-ray photon mean free path (MFP) in the photosphere:

$$l_\mu = (\mu)^{-1} = (\sigma_c \cdot n_e)^{-1}, \quad (51)$$

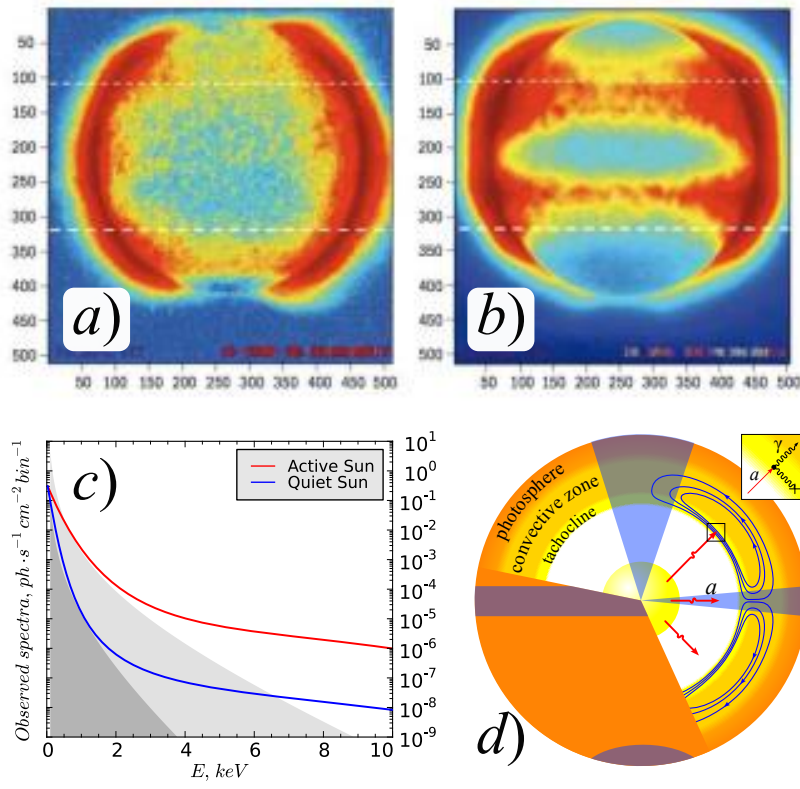


Fig. 10.— **Top:** Solar images at photon energies from 250 eV up to a few keV from the Japanese X-ray telescope Yohkoh (1991-2001) (adopted from [Zioutas et al. \(2009\)](#)). The following is shown: (a) a composite of 49 of the quietest solar periods during the solar minimum in 1996; (b) solar X-ray activity during the last maximum of the 11-year solar cycle. Most of the X-ray solar activity (right) occurs at a wide bandwidth of $\pm 45^\circ$ in latitude, being homogeneous in longitude. Note that $\sim 95\%$ of the solar magnetic activity covers this bandwidth.

Bottom: (c) Axion mechanism of solar irradiance variations above $2 \div 3$ keV, which is independent of the cascade reconnection processes in corona (see shaded areas and Fig. 9b,c,d), and the red and blue curves characterizing the irradiance increment in the active and quiet phases of the Sun, respectively;

(d) schematic picture of the radial travelling of the axions inside the Sun. Blue lines on the Sun designate the magnetic field. Near the tachocline (Fig. 5a) the axions are converted into γ -quanta, which form the experimentally observed Solar photon spectrum after passing the photosphere (Fig. 9). Solar axions that move towards the poles (blue cones) and in the equatorial plane (blue bandwidth) are not converted by Primakoff effect (inset: diagram of the inverse coherent process). The variations of the solar axions may be observed at the Earth by special detectors like the new generation CAST-helioscopes ([Irastorza et al. 2011](#)).

where μ is the total linear attenuation coefficient (cm^{-1}), the total Compton cross-section $\sigma_c = \sigma_0 = 8\pi r_0^2/3$ for the low-energy photons (Segrè 1953; Hodgson et al. 1997), n_e is the electrons density in the photosphere, and $r_0 = 2.8 \cdot 10^{-13} \text{ cm}$ is the so-called classical electron radius.

Taking into account the widely used value of the matter density in the solar photosphere $\rho \sim 10^{-7} \text{ g/cm}^3$ and supposing that it consists of the hydrogen (for the sake of the estimation only), we obtain that

$$n_e \approx \frac{\rho}{m_H} \approx 6 \cdot 10^{16} \text{ electron/cm}^3, \quad (52)$$

which yields the MFP of the photon (Segrè 1953; Hodgson et al. 1997)

$$l_\mu = (7 \cdot 10^{-25} \text{ cm}^2 \cdot 6 \cdot 10^{16} \text{ electron/cm}^3)^{-1} \approx 2.4 \cdot 10^7 \text{ cm} = 240 \text{ km}. \quad (53)$$

Since this value is smaller than the thickness of the solar photosphere ($l_{photo} \sim 300 \div 400 \text{ km}$), the Compton scattering is efficient enough to be detected at the Earth (see Fig. 11 and Fig. 9 adopted from Peres et al. (2000));

$$\frac{I_{\gamma \text{ photo}}}{I_{\gamma \text{ CZ}}} = \exp [-(\mu l)_{photo}] \sim 0.23, \quad (54)$$

which follows the particular case of the Compton scattering: Thomson differential and total cross section for unpolarized photons (Griffiths 1995).

And finally taking into account that $l_{chromo} \sim 2 \cdot 10^3 \text{ km}$ and $n_e \sim 10^{13} \text{ electron/cm}^3$ (i.e. $l_\mu \sim 1.4 \cdot 10^6 \text{ km}$) and $l_{corona} \sim 10^5 \text{ km}$ and $n_e < 10^{11} \text{ electron/cm}^3$ (i.e. $l_\mu > 1.4 \cdot 10^8 \text{ km}$) (Fig. 12.9 in Aschwanden et al. (2004)), one may calculate the relative intensity of the γ -quanta by Compton scattering in the solar corona

$$\frac{I_{\gamma \text{ corona}}}{I_{\gamma \text{ photo}}} = \frac{I_{\gamma \text{ chromo}}}{I_{\gamma \text{ photo}}} \cdot \frac{I_{\gamma \text{ corona}}}{I_{\gamma \text{ chromo}}} = \exp [-(\mu l)_{chromo}] \cdot \exp [-(\mu l)_{corona}] \approx 1, \quad (55)$$

which depends on the total relative intensity of γ -quanta (see Eq. (44)).

A brief summary is appropriate here. Coronal activity is a collection of plasma processes manifesting from the passage of magnetic fields through it from below, generated by the solar

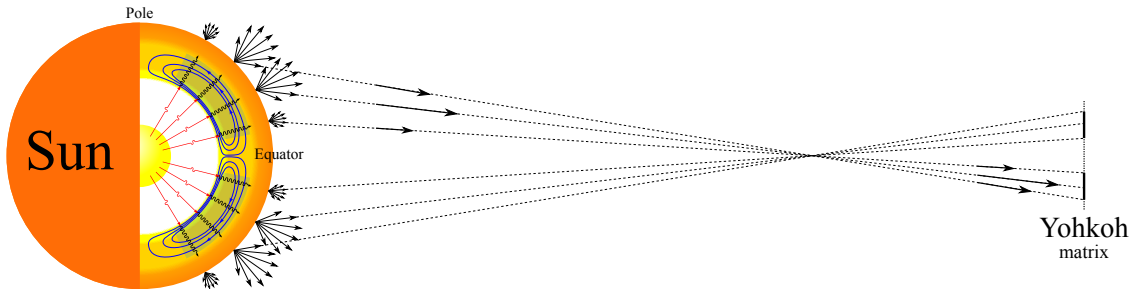


Fig. 11.— The formation of the high X-ray intensity bands on the Yohkoh matrix.

dynamo in cycles of approximately 11 years (Fig. 10). This global process culminating in the reversal of the solar magnetic dipole at the end of each cycle involves the turbulent dissipation of the magnetic energy, the flares and heating of the corona. The turbulent, highly dissipative, as well as largely ideal MHD processes play their distinct roles, each liberating a comparable amount of energy stored in the magnetic fields.

This mechanism is illustrated in Fig. 9d. When the magnetic flux erupts through the photosphere, it forms a pair of sunspots pushing the magnetic field up and aside. The magnetic field inside the sunspots is very high and the convection is suppressed. Therefore the coalescence of the magnetic field is also suppressed. When some magnetic field line crosses the region of the high Poynting flux, the energy is distributed along this line in the form of plasma heating. This makes such line visible in EUV band for some short time. While the magnetic field is being pushed to the sides, next field line crosses the region of high Poynting flux and flares up at the same position as the previous one and so on. This creates an illusion of a static flaring loop, while the magnetic field is in fact moving. It is interesting to note that [Chen et al. \(2015\)](#) expect the future investigation to show to what extent this scenario also holds for X-ray emission (see Supplementary Section 3 in [Chen et al. \(2015\)](#)).

In this context it is very important to consider the experimental observations of solar X-ray jets (e.g. solar space missions of Yohkoh and Hinode satellites), which show, for example, a gigantic coronal jet, ejecting from a compact active region in a coronal hole ([Shibata et al. 1994](#)) and tiny chromospheric anemone jets ([Shibata et al. 2007](#)).

These jets are believed to be an indirect proof of small-scale ubiquitous reconnection in the solar atmosphere and may play an important role in heating it, as conjectured by Parker ([Parker \(1988\)](#); [Zhang et al. \(2015\)](#); [Sterling et al. \(2015\)](#)).

Our main supposition here is that in contrast to EUV images (see orange line in Fig. 9d) and the coronal X-ray below $\sim 2 \div 3 \text{ keV}$, the hard X-ray emission above $\sim 3 \text{ keV}$ is in fact the γ -quanta of axion origin, born inside the magnetic tubes (see sunspot in Fig. 9d), and is not related to the mentioned indirect evidence (see e.g. Fig. 42 and Fig. 47 in [Shibata & Magara \(2011\)](#)) of the coronal jet, generated by the solar dynamo in cycles of approximately 11 years (Fig. 10). It will be interesting to see if the proposed picture will ultimately be confirmed, modified, or rejected by future observations and theoretical work to pin down the underlying physical ideas.

Taking into account the directional patterns of the resulting radiation as well as the fact that the maximum of the axion-originated X-ray radiation is situated near $30 - 40$ degrees of latitude (because of the solar magnetic field configuration), the mechanism of the high X-ray intensity bands formation on the Yohkoh matrix becomes obvious. The effect of these bands widening near the edges of the image is discussed in Appendix C in detail.

5. Summary and Conclusions

In the given paper we present a self-consistent model of the axion mechanism of the Sun’s luminosity variations, in the framework of which we estimate the values of the axion mass ($m_a \sim 3.2 \cdot 10^{-2} \text{ eV}$) and the axion coupling constant to photons ($g_{a\gamma} \sim 4.4 \cdot 10^{-11} \text{ GeV}^{-1}$). A good correspondence between the solar axion-photon oscillation parameters and the hadron axion-photon coupling derived from white dwarf cooling (see Fig. 8) is demonstrated.

One of the key ideas behind the axion mechanism of Sun luminosity variations is the effect of γ -quanta channeling along the magnetic flux tubes (waveguides inside the cool region) above the base of the Sun convective zone (Figs. 2, 4 and 5). The low refraction (i.e. the high transparency) of the thin magnetic flux tubes is achieved due to the ultrahigh magnetic pressure (Fig. 5a) induced by the magnetic field of about 4100 T (see Eq. (27) and Fig. 5a). So it may be concluded that the axion mechanism of Sun luminosity variations based on the lossless γ -quanta channeling along the magnetic tubes allows to explain the effect of the partial suppression of the convective heat transfer, and thus to understand the known puzzling darkness of the sunspots (see 2.2.1 in [Rempel & Schlichenmaier \(2011\)](#)).

It is shown that the axion mechanism of luminosity variations (which means that they are produced by adding the intensity variations of the γ -quanta of the axion origin to the coronal part of the solar spectrum (Fig. 10c)) easily explains the physics of the so-called Solar Equator – Poles effect observed in the form of the anomalous X-ray distribution over the surface of the active Sun, recorded by the Japanese X-ray telescope Yohkoh (Fig. 10, top).

The essence of this effect consists in the following: axions that move towards the poles (blue cones in Fig. 10, bottom) and equator (blue bandwidth in Fig. 10, bottom) are not transformed into γ -quanta by the inverse Primakoff effect, because the magnetic field vector is almost collinear to the axions’ momentum in these regions (see the inset in Fig. 10, bottom). Therefore the anomalous X-ray distribution over the surface of the active Sun is a kind of a “photo” of the regions where the axions’ momentum is orthogonal to the magnetic field vector in the solar overshoot tachocline. The solar Equator – Poles effect is not observed during the quiet phase of the Sun because of the magnetic field weakness in the overshoot tachocline, since the luminosity increment of the axion origin is extremely small in the quiet phase as compared to the active phase of the Sun.

In this sense, the experimental observation of the solar Equator – Poles effect is the most striking evidence of the axion mechanism of Sun luminosity variations. It is hard to imagine another model or considerations which would explain such anomalous X-ray radiation distribution over the active Sun surface just as well (compare Fig. 10a,b with Fig. B.1a).

And, finally, let us emphasize one essential and the most painful point of the present paper. It is related to the key problem of the axion mechanism of the solar luminosity variations and is stated rather simply: “Is the process of axion conversion into γ -quanta by the Primakoff effect really possible in the magnetic steps of an O-loop near the solar overshoot tachocline?” This question

is directly connected to the problem of the hollow magnetic flux tubes existence in the convective zone of the Sun, which are supposed to connect the tachocline with the photosphere. So, either the more general theory of the Sun or the experiment have to answer the question of whether there are the waveguides in the form of the hollow magnetic flux tubes in the cool region of the convective zone of the Sun, which are perfectly transparent for γ -quanta, or our model of the axion mechanism of Sun luminosity variations is built around simply guessed rules of calculation which do not reflect any real nature of things.

Acknowledgements

The work of M. Eingorn was supported by NSF CREST award HRD-1345219 and NASA grant NNX09AV07A.

A. Estimation of the hadron axion-photon coupling in white dwarf cooling

In order to estimate the parameters of the hadron axion-photon coupling

$$g_{a\gamma} \sim 4.4 \cdot 10^{-11} \text{ GeV}^{-1}, \quad m_a \sim 3.2 \cdot 10^{-2} \text{ eV} \quad (\text{A.1})$$

from white dwarf cooling, we focus on white dwarf stars (e.g. G117-B15A), which represent the final evolutionary stages of low- and intermediate-mass stars. Since they are strongly degenerate and do not have relevant nuclear energy sources, their evolution may be described as a slow cooling process in which the gravothermal energy release is the main energy source driving their evolution (e.g. [Córscico et al. \(2012\)](#)).

On the other hand, if there is dark matter in the Universe, some excellent candidates may exist in the galaxy and in the white dwarf stars in the form of weakly interacting particles, as it was recognized earlier e.g. by [Raffelt \(1986\)](#) for the case of axions.

In particular, stars can be used to put constraints on the mass of the axion ([Raffelt 1996](#)), where the coupling strength of KSVZ axions to electrons and to photons is defined through a dimensionless coupling constant g_{ae} , and dimension coupling constant $g_{a\gamma}$.

For example, from the so called radiatively induced coupling to electrons (e.g. Fig. 1 in [Srednicki \(1985\)](#), Fig. 1 in [Turner \(1990\)](#)):

$$(g_{ae})_{KSVZ} = \frac{3\alpha^2 m_e}{2\pi f_a} \left[\frac{E}{N} \ln \frac{f_a}{m_e} - \frac{2}{3} \frac{4+z+w}{1+z+w} \ln \frac{\Lambda_{QCD}}{m_e} \right], \quad (\text{A.2})$$

where $\alpha \simeq 1/137$ is the fine structure constant, $m_e = 0.511 \text{ MeV}$ is electron mass, f_a is the energy scale of the spontaneous breaking of the Peccei-Quinn U(1) symmetry, E/N is the ratio between the electromagnetic E and color N anomalies, the part proportional to $(4 + z + w)/(1 + z + w)$ arises from axion/pion mixing, and is cut off at the QCD confinement scale $\Lambda_{QCD} \approx 200 \text{ MeV}$, z and w are the quark mass ratios m_u/m_d and m_u/m_s introduced in equation of the axion mass

$$m_a = \frac{m_\pi f_\pi}{f_a} \sqrt{\frac{z}{(1+z+w)(1+z)}} \simeq 6 \text{ meV} \frac{10^9 \text{ GeV}}{f_a}, \quad (\text{A.3})$$

it is not difficult to derive

$$(g_{ae})_{KSVZ} \approx 8 \cdot 10^{-15}, \quad (\text{A.4})$$

where $m_\pi = 135 \text{ MeV}$ is the pion mass and $f_\pi \simeq 92 \text{ MeV}$ is the pion decay constant, $f_a \approx 1.85 \cdot 10^8 \text{ GeV}$, typical theoretical models with $|E/N - 1.95| = 7$ (see Fig. 8a).

The energy loss rate due to radiatively induced coupling of the hadronic axion to electrons (instead of the axion bremsstrahlung (Nakagawa et al. 1987, 1988)) as (4) is written

$$\varepsilon_{e \rightarrow a}^{WD} = 1.08 \cdot 10^{23} \frac{\text{erg}}{g \cdot s} \cdot \frac{(g_{ae}^2)_{KSVZ}}{4\pi} \cdot \frac{Z^2}{A} \cdot T_7^4 \cdot F(T, \rho), \quad (\text{A.5})$$

where Z and A are the atomic and mass numbers of the plasma components, $T_7 = T/10^7 \text{ K}$, F is a function of the temperature and the density which takes into account the properties of the plasma, and is of order unit throughout most of the interior of a typical white dwarf model (e.g. Bischoff-Kim et al. (2008)).

Consequently, it may be shown (see Eq.5 in Bischoff-Kim et al. (2008)) that the fraction of axion luminosity is then

$$L_{e \rightarrow a}^{WD} = \varepsilon_{e \rightarrow a}^{WD} \cdot M_* \simeq 1.03 \cdot 10^{57} \cdot \frac{(g_{ae}^2)_{KSVZ}}{4\pi} \text{ erg} \cdot s^{-1}, \quad (\text{A.6})$$

leading to the theoretical estimation of the axion fraction in the white dwarfs (stellar mass $M_* = 0.55 M_{Sun}$, effective temperature $T_{eff} = 12000 \text{ K}$ (established spectroscopically in Córscico et al. (2012)) and Sun luminosity

$$\log(L_{e \rightarrow a}^{WD}/L_{Sun}) \approx -5.8. \quad (\text{A.7})$$

Meanwhile, using the coupling constant $g_{a\gamma}$ (A.1), as in Fig. A.1a, it is evident that the hadron axion emission rate is a steeply falling function of density $\rho = 10^6 \text{ g/cm}^3$ when degeneracy effects become important (see Eq.(5.9) in Raffelt (1996)).

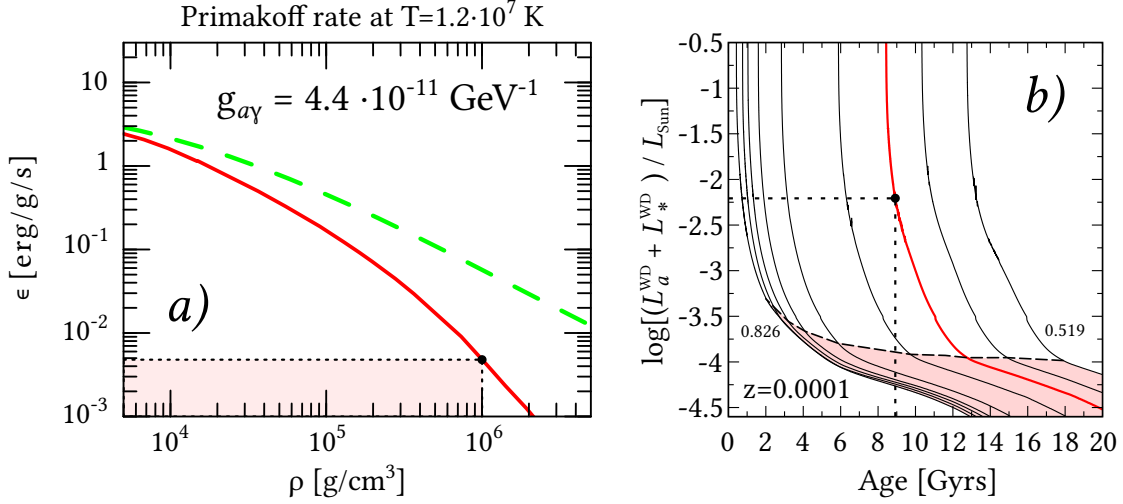


Fig. A.1.— (a) Energy-loss rate of a helium plasma at $T = 1.2 \cdot 10^7$ K of the pulsating white dwarf star G117B15A by axion emission with $g_{a\gamma} = 4.4 \cdot 10^{-11} \text{ GeV}^{-1}$. The solid line is from transverse-longitudinal fluctuations (degenerate, nonrelativistic); the dashed line is the corresponding classical (nondegenerate, nonrelativistic) limit (see Eq.(5.9) in Raffelt (1996)). (Adapted from Altherr et al. (1994)). (b) Total luminosity as a function of age for a set of sequences with four different metallicity of the progenitor star. The age corresponds to the total age of the model, by considering all the stages previous to the white dwarf cooling. The horizontal dashed line represents the point in the evolution where the crystallization process begins at the core, by means of the Horowitz et al. (2010) phase diagram for crystallization. The stellar mass values in solar mass units, from right to left, are: $M_*/M_{Sun} = 0.519, 0.534, 0.550, 0.561, 0.569, 0.621, 0.669, 0.708, 0.737$ and 0.826 for $Z = 0.0001$. (Adapted from Romero et al. (2015)).

Thus the total axion luminosity is

$$\log \frac{L_a^{WD}}{L_{Sun}} = \log \frac{L_{e \rightarrow a}^{WD} + L_{\gamma \rightarrow a}^{WD}}{L_{Sun}} \simeq \log \frac{L_{\gamma \rightarrow a}^{WD}}{L_{Sun}} = -2.3 \quad (\text{A.8})$$

where

$$\frac{L_{\gamma \rightarrow a}^{WD}}{L_{Sun}} \sim 4.7 \cdot 10^{-3}, \quad (\text{A.9})$$

for pulsating white dwarfs (e.g. G117-B15A with temperature $T \simeq 1.2 \cdot 10^7$ K and density $\rho = 10^6 \text{ g/cm}^3$ of isothermal core (Córscico et al. 2001) and the radius $R = 9.6 \cdot 10^8 \text{ cm}$ (Kepler et al. 2000), which yields (A.3)) is found using the Raffelt-DKTW-APG equation (see Fig.2 in Altherr

et al. (1994)) for the transition rate for a photon of energy E into an axion of the same energy (Dicus et al. 1980; Raffelt 1988; Altherr et al. 1994).

White dwarfs were used to constrain the axion-photon coupling (see (A.8) and Fig. A.1a), and it was noted that the somewhat large period decrease of the ZZ Ceti star G117-B15A, a pulsationally unstable white dwarf, could be ascribed to “invisible” axion cooling.

On the other hand, under assumptions valid for DAV pulsating white dwarfs (comprising “visible” cooling and gravitational contraction effects) to which G117-B15A belongs, i.e. that neutrino emission is negligible and the star is in the evolutionary stage prior to crystallization of its core, the luminosity is

$$L_*^{WD} = -\frac{dE_{thermal}}{dt} - \frac{dE_{grav}}{dt} \simeq 6.18 \cdot 10^{30} \text{ erg/s}, \quad (\text{A.10})$$

where, as commonly accepted, $E_{thermal}$ denotes the thermal energy of the star, and E_{grav} is the fraction of gravitational energy contributing to the luminosity (Biesiada & Malec 2004) experimentally measured by McCook & Sion (1999).

An interesting physical problem emerges in certain peripheric layers of such white dwarfs: does the possible appearance of the γ -quanta of axion origin, induced by the strong magnetic field in the tachocline via the thermomagnetic Ettingshausen-Nernst effect, produce the mixed “visible” gravothermal (see Eq.(A.10)) and “invisible” axion (see Eq.(A.8)) luminosity

$$\log \frac{L_a^{WD} + L_*^{WD}}{L_{Sun}} = ? \quad (\text{A.11})$$

In order approach this problem, let us first estimate the strong magnetic field in the tachocline.

Subject to a quasi-steady state characterized by a balance of the magnetic field of the dynamo, in the limit of weak collision, a thermomagnetic current can be generated in a (non)degenerate magnetized plasma. For a fully ionized hydrogen plasma with $Z = 1$ the generalized thermomagnetic Ettingshausen-Nernst effect leads to a current density (see Eqs. (12)-(19)) given by

$$j_y = -\frac{c}{B} \nabla p = -\frac{c}{B} \frac{dp}{dz}, \quad (\text{A.12})$$

where the pressure p corresponds to the overshoot tachocline (at the base of the convective envelope (see Eq. (20))).

From Maxwell’s equation $4\pi j_{\perp}/c = 4\pi j_y/c = \text{curl } B$, one has

$$j_y = \frac{c}{4\pi} \frac{dB}{dz} \quad (\text{A.13})$$

and thus by equating (A.12) and (A.13) we obtain as a result of integration in the limits $[B_{OT}, 0]$ in the left-hand side and $[0, p_{OT}]$ in the right-hand side:

$$\frac{B_{OT}^2}{8\pi} = p_{OT} \quad (\text{A.14})$$

where the pressure p_{OT} in overshoot tachocline (see Eq. (26)) is determined by the following cases:

$$p = \begin{cases} nk_B T, & \text{nonrelativistic ideal gas,} \\ K_1 \rho^{5/3}, & \text{nonrelativistic degenerate gas,} \\ K_2 \rho^{4/3}, & \text{relativistic degenerate gas.} \end{cases} \quad (\text{A.15})$$

From the astronomical data (Bhatia 2001) it is known that white dwarfs have a mass of solar order and planetary sizes, thus the density at the center is $10^5 \text{ g/cm}^3 \leq \rho_c \leq 10^6 \text{ g/cm}^3$, while on the periphery it is $10^2 \text{ g/cm}^3 \leq \rho_{periph} \leq 10^3 \text{ g/cm}^3$. This requires considering the quantum behavior of matter. Given that all atoms are ionized and so electrons are free, the physical assumption is that it is the pressure of this electron gas that balances the gravitational force (van Horn 1979). Such electron gas may be considered degenerate, since the temperature, corresponding to Fermi energy E_F is greater than that of the white dwarfs⁴.

Therefore, for a cold magnetic white dwarf the pressure of degenerate nonrelativistic electron plasma in (A.14) will be given by

$$p_{OT} = K_1 \rho^{5/3} = \frac{(3\pi^2)^{2/3}}{5} \cdot \frac{\hbar^2}{m_e(\mu_e m')^{5/3}} \cdot \rho^{5/3} \approx 3.12 \cdot 10^{12} \rho^{5/3} \text{ erg/cm}^3 \quad (\text{A.16})$$

where $m' = \mu_e m_p \approx 2m_p(\mu_e = A/Z \simeq 2)$ and m_p is the mass of the proton.

In this regard let us remind that the magnetic field of the thermomagnetic current (see Eq.(A.12)) in the overshoot tachocline neutralizes the magnetic field of the dynamo in core of the stars like ZZ Ceti G117-B15A.

We use the models of a stably burning hydrogen envelope on a helium core, obtained by solving the equations of hydrostatic balance, heat transport, energy generation, and mass conservation (e.g. Robinson et al. (1995); Steinfadt et al. (2010)). However, the most important feature between the H and He layers for our purposes is not only the chemical profile, but also the neutralization of the magnetic fields of the core on the core – envelope boundary.

Taking the mass density in the tachocline $\rho \leq 10^2 \text{ g/cm}^3$ we estimate the pressure of a degenerate non-relativistic electron plasma (A.16) as

⁴For example, the Fermi energy E_F of $\sim 1 \text{ MeV}$ yields $T \sim 10^{10} \text{ K}$, which is much greater than the usual internal temperature of such stars ($T \sim 10^7 \text{ K}$).

$$\frac{B_{OT}^2}{8\pi} = p_{OT} \leq 6.7 \cdot 10^{15} \text{ erg/cm}^3, \quad (\text{A.17})$$

where the poloidal magnetic field in tachocline gives rise to value

$$B_{OT} \leq 4.1 \cdot 10^4 \text{ T} = 4.1 \cdot 10^8 \text{ G}. \quad (\text{A.18})$$

Let us consider some properties of the anchored twisted magnetic flux tubes depending on the poloidal field in the tachocline through the shear flows instability development (see analogous Fig. 5a,b). A complete cooling of the O-loop inside the twisted magnetic tube near the tachocline leads to production of the γ -quanta of axion origin with the probability

$$P_{a \rightarrow \gamma}^{WD} = \frac{1}{4} (g_{a\gamma} B_{MS} L_{MS})^2 < 0.022. \quad (\text{A.19})$$

where $g_{a\gamma} = 4.4 \cdot 10^{-11} \text{ GeV}^{-1}$ is hadron axion coupling constant to photons (see Eq. A.3), $B_{MS} \leq B_z(0) \approx B_{OT}$ is the horizontal magnetic field of the O-loop (see Fig. 5a), $L_{MS} < d$ is the height of the magnetic shear steps, $d \leq 100 \text{ km}$ is the thickness of the tachocline in magnetic white dwarf (Kissin & Thompson 2015).

The theoretically estimated relative portion of the γ -quanta of axion origin is then

$$L_{a \rightarrow \gamma}^{WD} = P_{a \rightarrow \gamma}^{WD} L_a^{WD} < 0.022 \cdot 4.7 \cdot 10^{-3} L_{Sun} \simeq 10^{29} \text{ erg/s}, \quad (\text{A.20})$$

which is in agreement with the experimental one (see Fig. A.2b). Since it is rather small, the total luminosity is the sum of the “visible” gravothermal (see Eq. (A.10)) and “invisible” axion (see Eq. (A.8)) components

$$\log \frac{L_a^{WD} + L_*^{WD}}{L_{Sun}} \simeq -2.2. \quad (\text{A.21})$$

As a result, following our aim, we determined the parameters of hadron axion-photon coupling (A.3) and derived several important parameters from white dwarf cooling (G117-B15A):

- **Luminosity.** Total luminosity (A.21), depending on the axion luminosity through energy-loss rate of a helium plasma at $T = 1.2 \cdot 10^7 \text{ K}$ of the pulsating white dwarf star G117-B15A by axion emission with $g_{a\gamma} = 4.4 \cdot 10^{-11} \text{ GeV}^{-1}$ (Fig. A.1a) and gravothermal luminosity, experimentally measured by McCook & Sion (1999), coincides with the observed pulsating white dwarf stars lying in three strips in the H-R diagram (see Fig. A.2c). Adopted from Winget & Kepler (2008)). We gave the estimated parameters of the pulsating DAV white dwarf, or ZZ Ceti star, G117-B15A, which enter the ZZ Ceti variable (DAV) instability

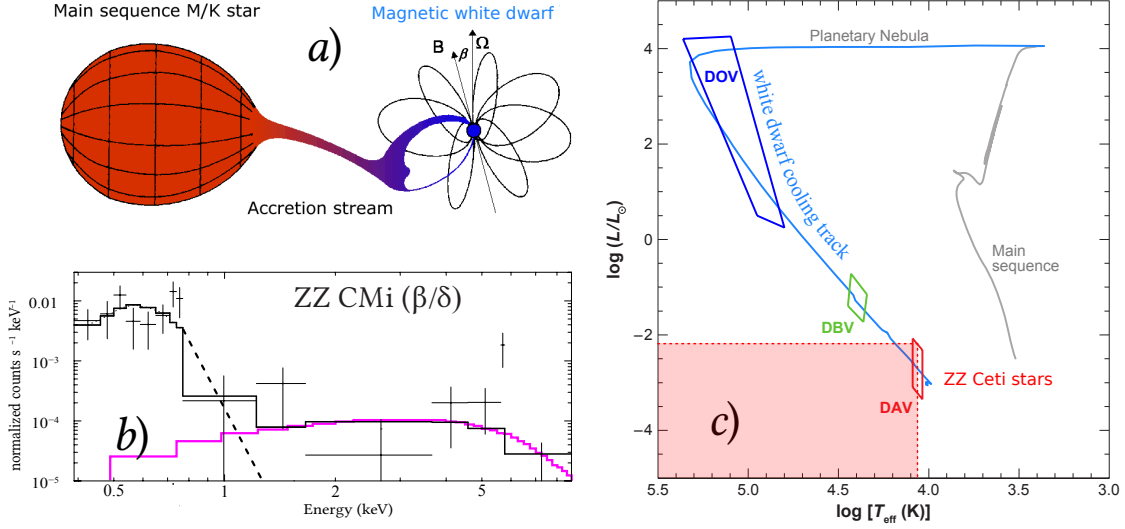


Fig. A.2.— (a) Schematic of binary system. The red dwarf secondary loses gas which accretes onto the strongly magnetic white dwarf via an accretion stream. At some point between the two stars the energy density of the magnetic field is sufficient to redirect the flow so that accretion takes place near or at the magnetic pole. (Adapted from Cropper (1990)). (b) Swift/XRT spectra of the WD symbiotic with newly discovered X-ray emission together with their X-ray spectral types ZZ CMi. The full line shows the best-fit model (black line), while the dotted line shows the contribution of the individual spectral components in the case of multi-component models. (Adapted from Luna et al. (2013)). X-ray emission (rose line) is the γ -quanta of axion origin coming from the magnetic tubes, anchored in tachocline of white dwarf ZZ CMi. (c) The observed pulsating white dwarf stars lie in three strips in the H-R diagram (adopted from Winget & Kepler (2008)). The estimates of the pulsating DAV white dwarf (like ZZ Ceti star, G117-B15A) parameters are shown here. They enter the ZZ Ceti variable (DAV) instability region, a discrete strip in the $\log(T_{eff}(K)) - \log(L/L_{Sun})$ plane that spans $T_{eff} \sim 12000$ K at $\log(L/L_{Sun}) = -2.2$ (red dotted line).

region, a discrete strip in the $\log(T_{eff}(K)) - \log(L/L_{Sun})$ plane that spans $T_{eff} \sim 12000\ K$ at $\log(L/L_{Sun}) = -2.2$.

- **Magnetic field and age.** Strong magnetic field $B_{OT} \sim 4.1 \cdot 10^8\ G$, produced in the tachocline by the thermomagnetic Ettingshausen-Nernst effect, and age of G117-B15A, when the total luminosity begins to decay ($10^9\ yr$) in a $0.55 M_{Sun}$ (see Fig. A.1b), agree with the theoretical estimates of the magnetic field and age of magnetic white dwarfs (Kissin & Thompson 2015).
- **Darkspots by analogy to sunspots.** The spectroscopic observations in white dwarfs, showed the variations of equivalent width in the Balmer lines, proposing that these variations are due to a star-spot (or darkspot) on the magnetic white dwarfs, analogous to a sunspot, which is affecting the temperature at the surface, and therefore its photometric magnitude (Brinkworth et al. 2005; Valyavin et al. 2011, 2014). According to previous studies, this variability can be explained by the presence of a dark spot having a magnetic nature, analogous to a sunspot. Motivated by this idea, astrophysicists examine possible physical relationships between the suggested dark spot and the strong-field magnetic structure (magnetic “spot” or “tube”) recently identified on the surface of this star (Maxted et al. 2000; Valyavin et al. 2011, 2014).

It is generally believed (Valyavin et al. 2014), that the magnetic field suppresses atmospheric convection, leading to dark spots in the most magnetized areas. Valyavin et al. (2014) also found that strong fields are sufficient to suppress convection over the entire surface in cool magnetic white dwarfs, which inhibits their cooling evolution relative to weakly magnetic and non-magnetic white dwarfs, making them appear younger than they truly are. Still it should be kept in mind that this is only a supposition, and not a strict proof, since the problem of generation and transport of energy by magnetic flux tubes remains unsolved.

In the present paper we show how the problem of energy transport by magnetic flux tubes and darkspots formation may be solved by analogy to sunspot by the Parker-Biermann cooling effect (see Section 3.1.2). Here we imply a theoretical possibility of the time variation of the darkspot activity to correlate with the flux of the γ -quanta of axion origin, which are produced within almost horizontal magnetic field of O-loop inside the magnetic tube (see Fig. 5a).

Because the convection in the convection zone is partial (i.e. it only works between the cool region of magnetic tube (see Fig. 5a) and the surface of magnetic white dwarf), the axion mechanism based on the lossless γ -quanta “channeling” along the magnetic tubes allows to explain the effect of the almost complete suppression of the convective heat transfer, and thus to understand the known puzzling darkness of the starspots (by analogy to the sunspots in Rempel & Schlichenmaier (2011)).

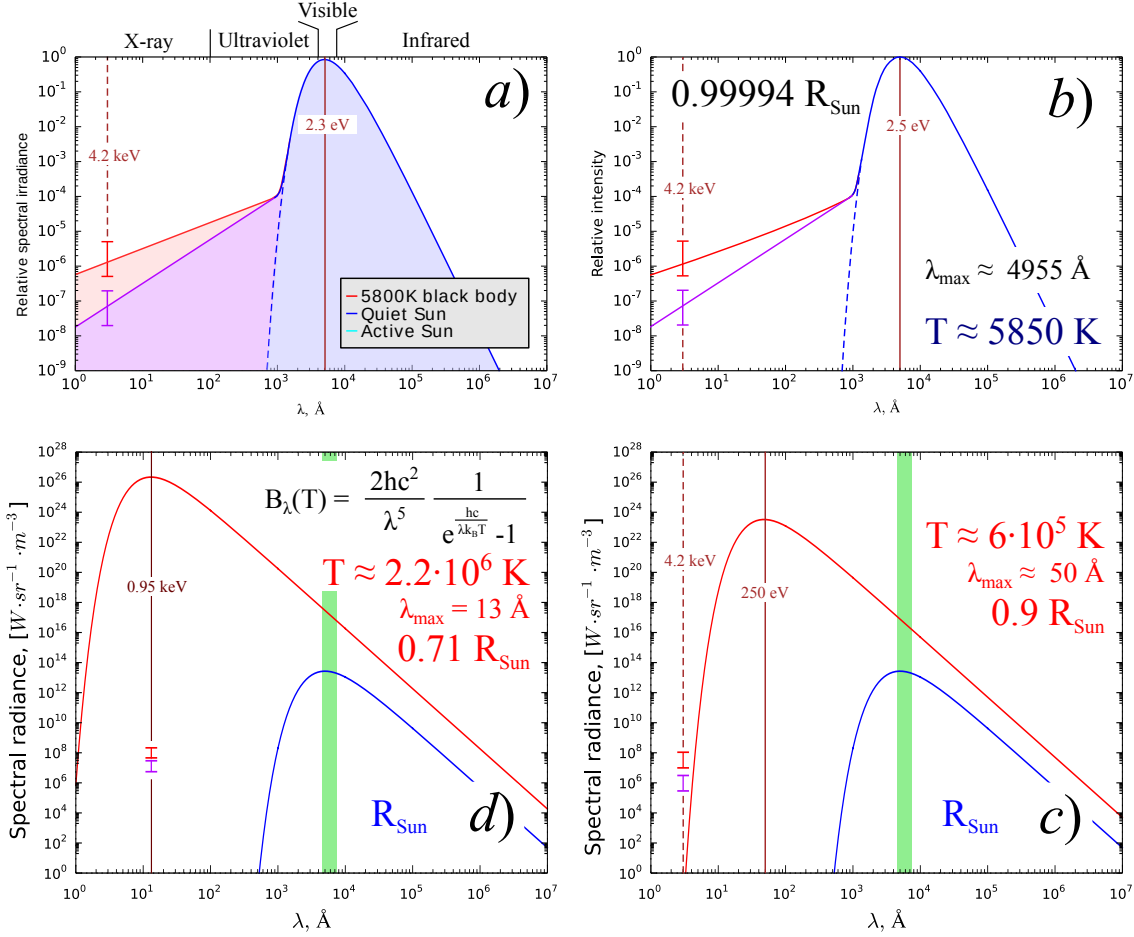


Fig. B.1.— a) The smoothed Solar spectrum corresponds to a black body with a temperature $5.77 \cdot 10^3$ K at R_{Sun} (see Fig. 11 in Zioutas et al. (2009)). The red and violet bars represent the high and low contributions from the X-rays of axion origin with mean energy of 4.2 keV born in the “magnetic steps” at $\sim 0.72R_{Sun}$, roughly estimated for the solar cycle 22. It is possible to perform similar estimations for any other solar cycle using the Eqs. (19), (44), (B.3) and the data from Dikpati et al. (2008); Pevtsov et al. (2014); Lockwood (2001). Note that these X-ray contributions exist within the magnetic tubes only.

b) A spectrum of a black body with a temperature 5850 K at $0.99994R_{Sun}$ (see Fig. 7). The X-ray luminosity (high intensity red and low intensity violet lines) is determined by the Compton scattering of the mentioned 4.2 keV.

c) Red line is a spectrum of a black body with a temperature $6 \cdot 10^5$ K at $0.9R_{Sun}$ (see Fig. 7 and Bahcall & Pinsonneault (1992)). The high and low X-ray luminosity (red and violet bars) are determined by the 4.2 keV X-rays which propagate along the cool region of the magnetic tube without scattering (Fig. 5a). Blue line corresponds to the black-body spectrum of the solar surface.

d) A spectrum of a black body with a temperature $2.22 \cdot 10^6$ K at $0.71R_{Sun}$ (see Fig. 7 and Bahcall & Pinsonneault (1992)). The X-ray luminosity is determined by the average energy ~ 0.95 keV thermal photons only (in tachocline (Bailey et al. 2009)). These photons are converted into axions in “magnetic steps” at $\sim 0.72R_{Sun}$, and thus do not constitute the spectra of the higher layers. As above, the blue line corresponds to the black-body spectrum of the solar surface.

B. X-ray coronal luminosity variations

The X-ray luminosity of the Solar corona during the active phase of the solar cycle is defined by the following expression:

$$(L_{corona}^X)_{max} = \int_{X-ray} \frac{d\Phi_{corona}^{max}(E)}{dE} \cdot E dE = \int_{X-ray} \frac{dW_{corona}^{max}(E)}{dE} dE. \quad (B.1)$$

In the quiet phase it may be written as

$$(L_{corona}^X)_{min} = \int_{X-ray} \frac{d\Phi_{corona}^{min}(E)}{dE} \cdot E dE = \int_{X-ray} \frac{dW_{corona}^{min}(E)}{dE} dE. \quad (B.2)$$

Then integrating the blue curve in Fig. B.1 for $(L_{corona}^X)_{max}$ and the cyan curve for $(L_{corona}^X)_{min}$, we obtain

$$\frac{(L_{corona}^X)_{min}}{L_{Sun}} \sim 10^{-7}; \quad \frac{(L_{corona}^X)_{max}}{L_{Sun}} \sim 10^{-6}. \quad (B.3)$$

So it may be derived from here that the Sun's luminosity is quite low in X-rays (B.3), typically (see Rieutord (2014)),

$$10^{-7} L_{Sun} \leq L_{corona}^X \leq 10^{-6} L_{Sun}, \quad (B.4)$$

but it varies with the cycle (see blue and cyan lines in Fig. B.1a) as nicely shown by the pictures obtained with the Yohkoh satellite (see Fig. 4 in Rieutord (2014)).

And finally, it may be supposed that X-rays, propagating from the tachocline towards the photosphere, interact with the charged particles via the Compton scattering, but only outside the magnetic tubes. The axion-originated X-ray radiation channeling inside the magnetic tubes does not experience the Compton scattering up to the photosphere (Figure B.1).

C. Explanation of the high X-ray intensity bands widening near the Yohkoh image edges

It is interesting to note that the bands of high X-ray intensity on Yohkoh images deviate from the solar parallels (Fig. 10b). This is especially the case near the edges of the visible solar disk.

This effect may be explained graphically by means of figures C.1 and C.2. These figures show the schematic concept of the Sun image formation on the Yohkoh matrix. Fig. C.1 shows the Sun from its pole.

Let us choose three sectors of equal size on the surface of the Sun (Fig. C.1, C.2). The areas of the photosphere cut by these sectors are also equal ($S_0 = S_1 = S_2$). However, as it is easily seen in the suggested scheme, the *projections* of these sectors on the Yohkoh matrix are not of equal area (Fig. C.1, C.2). The S'_1 and S'_2 projections areas are much less than that of the S'_0 projection (Fig. C.1). It means that the radiation emitted by the sectors S_1 and S_2 of the solar photosphere and captured by the satellite camera will be concentrated within *less* area (near the edges of the solar disk) than the radiation coming from the S_0 sector (in the center of the solar disk). As a

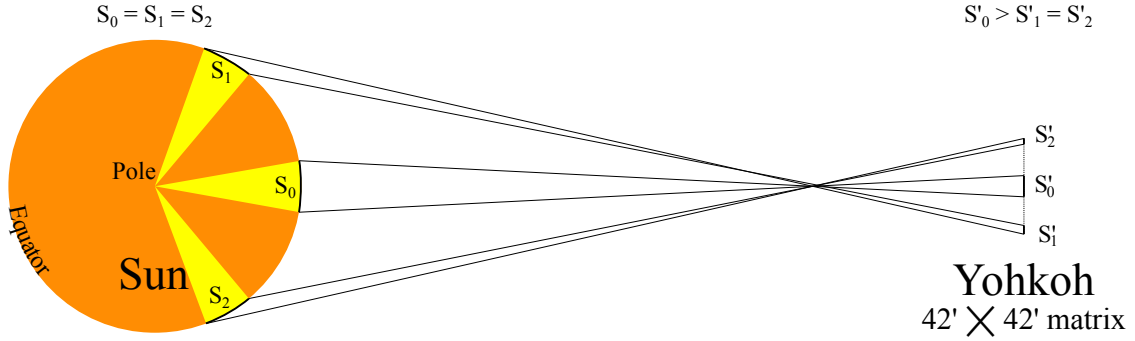


Fig. C.1.— A sketch of the Sun image formation on the Yohkoh matrix.

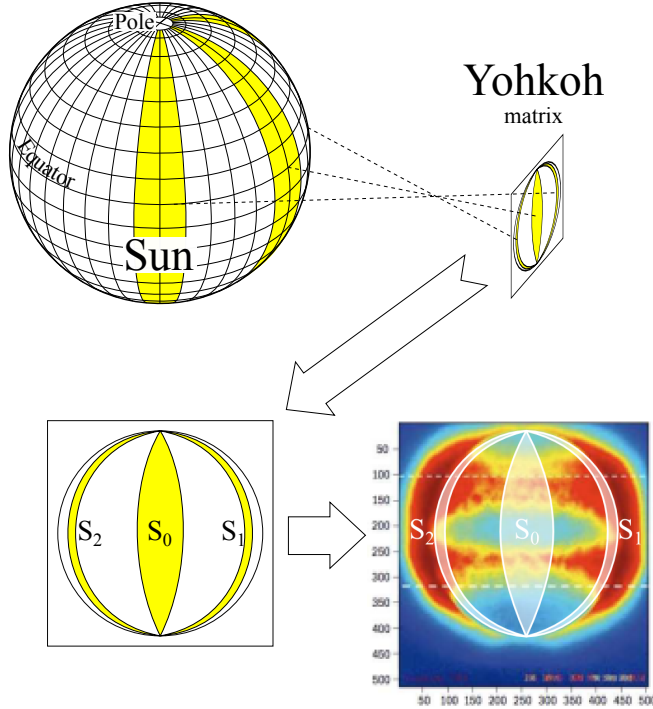


Fig. C.2.— A sketch of the Sun image formation on the Yohkoh matrix.

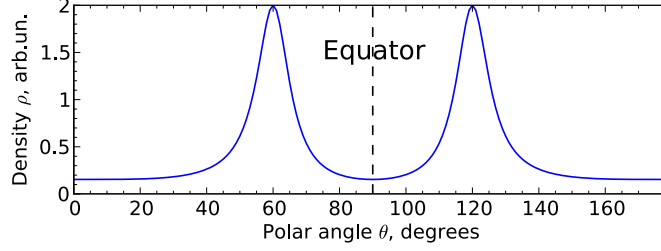


Fig. C.3.— Graphical representation of Eq. (C.1).

result, the satellite shows higher intensity near the image edges than that in the center, in spite of the obvious fact that the real radiation intensity is equal along the parallel of the Sun.

Therefore, because of the system geometry, the satellite tends to “amplify” the intensity near the image edges, and the areas that correspond to the yellow and green areas at the center (Fig. 10b) become red near the edges, thus leading to a visible widening of the high intensity bands.

A particularly high radiation intensity near the very edges of the visible solar disk, observed even during the quiet phase of the Sun (Fig. 10a), indicates a rather “wide” directional radiation pattern of the solar X-rays.

Let us make a simple computational experiment. We will choose a sphere of a unit radius and spread the points over its surface in such a way that their density changes smoothly according to some dependence of the *polar* angle (θ). The *azimuth* angle will not influence the density of these points. For this purpose any function that provides a smooth change of the density will do. For example, this one:

$$\rho(\theta) = [\rho_0 + \rho_{max} \cdot \cos(2 \cos \theta)]^{-1}. \quad (\text{C.1})$$

Here we take $\rho_0 = 3.5$ and $\rho_{max} = 3$ in arbitrary units. The graphical representation of this dependence is shown in Fig. C.3.

I.e. it yields a minimum density of the points near the poles and the equator, and the maximum density of the points near $\theta = 60^\circ$ and $\theta = 120^\circ$.

The polar angle θ was set in the range $[0, 180^\circ]$ with the step of 1° . The azimuth angle φ was set in the range $[0, 180^\circ]$ (one hemisphere) with a variable step $\Delta\varphi$ representing the variable density, since the points density is inversely proportional to the step between them ($\Delta\varphi \sim 1/\rho$). We assume that

$$\Delta\varphi(\theta) = \Delta\varphi_0 + \Delta\varphi_{max} \cdot \cos(2 \cos \theta) \text{ [deg]}. \quad (\text{C.2})$$

The values of $\Delta\varphi_0 = 3.5^\circ$ and $\Delta\varphi_{max} = 3^\circ$ were chosen arbitrarily. So,

$$\Delta\varphi(\theta) = 3.5 + 3 \cdot \cos(2 \cos \theta) \text{ [deg]}. \quad (\text{C.3})$$

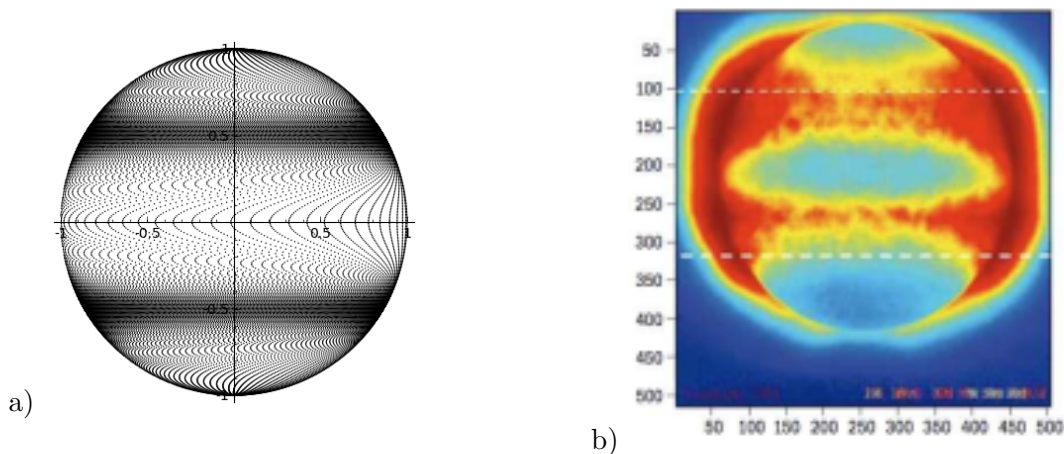


Fig. C.4.— a) Simulation of the high intensity bands formation on the 2D projection of the sphere. b) Sun X-ray image from Yohkoh satellite during the active phase of the Sun.

From Eq. (C.3) it is clear that the minimum step was 0.5° and the maximum step was 6.5° . Apparently, the more is the step, the less is the density (near the poles and the equator) and vice versa, the less is the step, the more is the points density. This was the way of providing a smooth change of the points density by latitude (along the solar meridians).

Obviously, this forms the “belts” of high density of the points along the parallels. The projection of such sphere on any plane perpendicular to its equator plane will have the form shown in Fig. C.4a. As it is seen in this figure, although the density does not depend on azimuth angle, there is a high density bands widening near the edges of the *projected* image. These bands are similar to those observed on the images of the Sun in Fig. C.4b.

Let us emphasize that the exact form of the dependence (C.2) as well as the exact values of its parameters were chosen absolutely arbitrarily for the sole purpose of the qualitative effect demonstration. They have no relation to the actual latitudinal X-ray intensity distribution over the surface of the Sun.

REFERENCES

- Adler, S., Gamboa, J., Mendez, F., & Lopez-Sarrior, J. 2008, *Annals Phys.*, 32, 2851
- Alfvén, H. 1942, *Nature*, 150, 405
- Altherr, T., Petitgirard, E., & del Río-Gaztelurrutia, T. 1994, *Astroparticle Physics*, 2, 175
- Andriamonje, S., et al. 2007, *J. Cosmol. Astropart. Phys.*, 10, 0702, [arXiv:hep-ex/0702006](#)
- Arias, P., Cadamuro, D., Goodsell, M., et al. 2012, *JCAP*, 13, [arXiv:1201.5902](#)

- Arik, E., Aune, S., Autiero, D., et al. 2009, *Journal of Cosmology and Astroparticle Physics*, 2009, 008
- Arik, M., Aune, S., Barth, K., et al. 2013, [arXiv:1307.1985](#)
- . 2011, *Phys. Rev. Lett.*, 107, 261302
- Aschwanden, M. 2011, *Self-Organized Criticality in Astrophysics* (Springer-Verlag Berlin Heidelberg), 416
- Aschwanden, M. J. 2014, *The Astrophysical Journal*, 782, 54
- Aschwanden, M. J., Alexander, D., & DeRosa, M. L. 2004, *Solar and Space Weather Radiophysics: Current Status and Future Developments*, ed. D. E. Gary & C. U. Keller (Boston/Dordrecht/London: Kluwer Academic Publishers), 243264
- Asztalos, S. J., Carosi, G., Hagmann, C., et al. 2010, *Phys. Rev. Lett.*, 104, 041301
- Ayala, A., Domínguez, I., Giannotti, M., Mirizzi, A., & Straniero, O. 2014, *Phys. Rev. Lett.*, 113, 191302
- Baer, H., Lessa, A., Rajagopalan, S., & Sreethawong, W. 2011, *JCAP*, 31
- Bahcall, J., & Pinsonneault, M. 1992, *Rev. Mod. Phys.*, 64, 885
- Bahcall, J. N., & Pinsonneault, M. H. 2004, *Phys. Rev. Lett.*, 92, 121301, [arXiv:astro-ph/0402114](#)
- Bailey, J. E., Rochau, G. A., Mancini, R. C., et al. 2009, *Physics of Plasmas*, 16, 058101
- Bak, P. 1996, *How Nature Works: the science of self-organized criticality* (Springer New York)
- Bak, P., & Chen, K. 1989, *Physica D: Nonlinear Phenomena*, 38, 5
- Bak, P., Tang, C., & Wiesenfeld, K. 1987, *Physical Review Letters*, 59, 381
- Bak, P., Tang, C., & Wiesenfeld, K. 1988, *Phys. Rev. A*, 38, 364
- Benz, A. 2008, *Living Rev. Solar Phys.*, 5, 1
- Bhatia, V. B. 2001, *Textbook of astronomy and astrophysics with elements of cosmology* (Pangbourne, India : Alpha Science International Ltd)
- Biermann, L. 1941, *Vierteljahrsschrift Astron. Gesellsch.*, 76, 194
- Biesiada, M., & Malec, B. 2004, *MNRAS*, 350, 644
- Bischoff-Kim, A., Montgomery, M. H., & Winget, D. E. 2008, *ApJ*, 675, 1512
- Brinkworth, C. S., Marsh, T. R., Morales-Rueda, L., et al. 2005, *MNRAS*, 357, 333

- Cadamuro, D. 2012, PhD thesis, der Fakultät für Physik der Ludwig-Maximilians-Universität München, München, [arXiv:1210.3196](#)
- Caligari, P., Schuessler, M., & Moreno-Inertis, F. 1981, *Astrophys. J.*, 243, 309
- Carosi, G., Friedland, A., Giannotti, M., et al. 2013, [arXiv:1309.7035](#)
- Charbonneau, P., McIntosh, S., Liu, H.-L., & Bogdan, T. 2001, *Solar Physics*, 203, 321
- Chen, F., Peter, H., Bingert, S., & Cheung, M. C. M. 2015, *Nature Physics*, 11, 492
- Chitre, S. 1963, *Monthly Notices Roy Astron. Soc.*, 126, 431
- Córsico, A. H., Althaus, L. G., Miller Bertolami, M. M., et al. 2012, *Monthly Notices of the Royal Astronomical Society*, 424, 2792
- Córsico, A. H., Benvenuto, O. G., Althaus, L. G., Isern, J., & Garcá-Berro, E. 2001, *New Astronomy*, 6, 197
- Couvidat, S., Turck-Chize, S., & Kosovichev, A. G. 2003, *The Astrophysical Journal*, 599, 1434
- Cranmer, S. R. 2015, University of Colorado ASTR-3760 course, *Solar and Space Physics*
- Cropper, M. 1990, *Space Sci. Rev.*, 54, 195
- Csaki, C., Kaloper, N., & Terning, J. 2002, *Phys. Rev. Lett.*, 88, 161302, [arXiv:astro-ph/0111311](#)
- D. Stamatellos, A. P. Whitworth, T. Bisbas, & S. Goodwin. 2007, *A&A*, 475, 37
- De Angelis, A., Galanti, G., & Roncadelli, M. 2011, *Phys. Rev. D*, 84, 105030
- Dicus, D. A., Kolb, E. W., Teplitz, V. L., & Wagoner, R. V. 1980, *Phys. Rev. D*, 22, 839
- Dikpati, M., Gilman, P., & de Toma, G. 2008, *The Astrophysical Journal*, 673, L99
- Dine, M., Fischler, W., & Srednicki, M. 1981, *Physics Letters B*, 104, 199
- Ettingshausen, A. V., & Nernst, W. 1886, *Wied. Ann.*, 29, 343
- Fairbairn, M., Rashba, T., & Troitsky, S. 2011, *Phys. Rev. D*, 84, 125019
- Fan, Y. 2009, *Living Rev.Solar Phys.*, 6, 4
- Fan, Y., & Fisher, G. 1996, *Solar Phys.*, 166, 17
- Fawzy, D., & Cuntz, M. 2011, *Astron. Astrophys.*, 521, A91
- Fawzy, D., Cuntz, M., & Rammacher, W. 2012, *Mon. Not. R. Astron. Soc.*, 426, 1916
- Ferguson, J. W., Alexander, D. R., Allard, F., et al. 2005, *ApJ*, 623, 585

- Fisher, G., Fan, Y., Longcope, D., Linton, M., & Pevtsov, A. 2000, *Solar phys.*, 192, 119, (Invited Review)
- Fowler, W. A., Burbidge, G. R., & Burbidge, E. M. 1955, *Astrophysical Journal Supplement*, 2, 167
- Friedland, A., Giannotti, M., & Wise, M. 2013, *Phys. Rev. Lett.*, 110, 061101
- Gold, T., & Hoyle, F. 1960, *Monthly Notices of the Royal Astronomical Society*, 120, 89
- Golub, L., Rosner, R., Vaiana, G., & Weiss, N. 1981, *Astrophys. J.*, 243, 309
- Gough, D. 2010, in *Magnetic Coupling between the Interior and Atmosphere of the Sun*, ed. S. Hasan & R. J. Rutten, *Astrophysics and Space Science Proceedings* (Springer Berlin Heidelberg), 37–66
- Griffiths, D. 1995, *Introduction to Quantum Mechanics* (Prentice Hall)
- Guendelman, E. I., Shilon, I., Cantatore, G., & Zioutas, K. 2009, [arXiv:0906.2537](#)
- Hassan, S. 2003, *Lecture Notes in Physics*, 619, 173
- Hochmuth, K., & Sigl, G. 2007, *Phys.Rev. D*, 76, 123011
- Hodgson, P., Gadioli, E., & Erba, E. 1997, *Introductory nuclear physics*, Oxford science publications (Clarendon Press)
- Hollweg, J. 1990, in *Physics of Magnetic Flux Ropes*, ed. C. Russell, E. Priest, & L. Lee, *Geophys. Monograph No. 58* (Washington, 23: American Geophysical Union)
- Horowitz, C. J., Schneider, A. S., & Berry, D. K. 2010, *Phys. Rev. Lett.*, 104, 231101
- Hoyle, F. 1949, *Some Recent Researches in Solar Physics* (Cambridge University Press)
- Ilonidis, S., Zhao, J., & Kosovichev, A. 2011, *Nature*, 333, 993
- Irastorza, I. G. 2013, *The International Axion Observatory IAXO. Letter of Intent to the CERN SPS committee*, Tech. Rep. CERN-SPSC-2013-022. SPSC-I-242, CERN, Geneva
- Irastorza, I. G., Avignone, F. T., Caspi, S., et al. 2011, *Journal of Cosmology and Astroparticle Physics*, 2011, 013
- Isern, J., Garcia-Berro, E., Torres, S., & S., C. 2008, *The Astrophysical Journal*, 682, L109
- Kepler, S., Mukadam, A., Winget, D., et al. 2000, *Astrophysical Journal Letters*, 534, L185
- Kim, J. 1979, *Phys. Rev. Lett.*, 43, 103
- Kim, J. E., & Carosi, G. 2010, *Reviews of Modern Physics*, 82

- Kim, Y. B., & Stephen, M. J. 1969, in *Superconductivity*, ed. R. Parks, Vol. 2 (New York: Dekker)
- Kissin, Y., & Thompson, C. 2015, *The Astrophysical Journal*, 809, 108
- Lockwood, M. 2001, *Journal of Geophysical Research: Space Physics*, 106, 16021
- Lu, E. T., & Hamilton, R. J. 1991, *ApJ*, 380, L89
- Lu, E. T., Hamilton, R. J., McTiernan, J. M., & Bromund, K. R. 1993, *ApJ*, 412, 841
- Luna, G. J. M., Sokoloski, J. L., Mukai, K., & Nelson, T. 2013, *A&A*, 559, A6
- Masso, E. 2008, *Lect. Notes Phys.*, 741, 83
- Maxted, P. F. L., Ferrario, L., Marsh, T. R., & Wickramasinghe, D. T. 2000, *MNRAS*, 315, L41
- McCook, G. P., & Sion, E. M. 1999, *ApJS*, 121, 1
- Mirizzi, A., Raffelt, G. G., & Serpico, P. D. 2005, *Phys. Rev. D*, 72, 023501
- Moreno-Insertis, F. 1982, *Astron. Astrophys.*, 122, 241
- Nakagawa, M., Adachi, T., Kohyama, Y., & Itoh, N. 1988, *ApJ*, 326, 241
- Nakagawa, M., Kohyama, Y., & Itoh, N. 1987, *ApJ*, 322, 291
- Nelson, N. J., & Miesch, M. S. 2014, *Plasma Physics and Controlled Fusion*, 56, 064004
- Parker, E. N. 1955a, *Astrophys. J.*, 121, 491
- . 1955b, *Astrophysics J.*, 122, 293
- . 1979a, *Cosmical magnetic fields: Their origin and their activity* (Oxford, Clarendon Press), 858
- . 1979b, *Astrophys. J.*, 230, 905
- . 1988, *ApJ*, 330, 474
- . 1993, *The Astrophysical Journal*, 408, 707
- . 1994, *The Astrophysics Journal*, 433, 867
- Peres, G., Orlando, S., Reale, Rosner, R., & Hudson, H. 2000, *The Astrophys. J.*, 528, 537
- Pevtsov, A. A., Bertello, L., Tlatov, A. G., et al. 2014, *Solar Physics*, 289, 593
- Pevtsov, A. A., Nagovitsyn, Y. A., Tlatov, A. G., & Rybak, A. L. 2011, *The Astrophysical Journal Letters*, 742, L36
- Priest, E., & Forbes, T. 2000, *Magnetic reconnection. MHD theory and applications* (Cambridge University Press)

- Primakoff, H. 1951, Phys. Rev., 81, 899
- Raffelt, G., & Stodolsky, L. 1988, Phys. Rev. D, 37, 1237
- Raffelt, G. G. 1986, Physics Letters B, 166, 402
- . 1988, Phys. Rev. D, 37, 1356
- . 1996, Stars as Laboratories for Fundamental Physics. The Astrophysics of Neutrinos, Axions, and Other Weakly Interacting Particles (University of Chicago Press)
- . 2004, Phys. Lett., 592, 391
- . 2008, Lect. Notes Phys., 741, 51, [arXiv:hep-ph/0611350](#)
- Redondo, J., & Ringwald, A. 2010, [arXiv:1011.3741 \[hep-ph\]](#)
- Rempel, M. 2011, The Astrophysical Journal, 740, 15
- Rempel, M., & Schlichenmaier, R. 2011, Living Rev. Solar Phys., 8
- Rieutord, M. 2014, in Société Française d’Astronomie et d’Astrophysique (SF2A), [arXiv:1410.3725](#)
- Roberts, B. 1991, Geophys. Astrophys. Fluid Dyn., 62, 83
- Roberts, B., & Ulmschneider, P. 1997, in Lecture Notes in Physics, Vol. 489, Solar and Heliospheric Plasma Physics, ed. G. Simnett, C. Alissandrakis, & L. Vlahos (Springer Berlin Heidelberg), 75–101
- Robinson, E. L., Mailloux, T. M., Zhang, E., et al. 1995, ApJ, 438, 908
- Rogers, F. J., & Iglesias, C. A. 1994, Science, 263, 50
- Romero, A. D., Campos, F., & Kepler, S. O. 2015, Monthly Notices of the Royal Astronomical Society, 450, 3708
- Ruzmaikin, A. 2000, Solar phys., 192, 49, (Invited Review)
- Schwarzschild, M. 1958, Structure and evolution of the stars (Princeton, Princeton University Press)
- Segrè, E., ed. 1953, Experimental Nuclear physics, Vol. 1 (New York: John Wiley & Sons)
- Shibata, K., & Magara, T. 2011, Living Reviews in Solar Physics, 8, doi:10.12942/lrsp-2011-6
- Shibata, K., Nitta, N., Strong, K. T., et al. 1994, ApJ, 431, L51
- Shibata, K., Nakamura, T., Matsumoto, T., et al. 2007, Science, 318, 1591
- Shifman, M., Vainshtein, A., & Zakharov, V. 1980, Nucl. Phys. B, 166, 493

- Sondheimer, E. H. 1948, Proceedings of the Royal Society of London. Series A, Mathematical and Physical Sciences, 193, 484
- Spitzer, L. J. 1956, Physics of Fully Ionized Gases (New York: John Wiley & Sons, Inc.)
- . 1962, Physics of Fully Ionized Gases, 2nd edn. (New York: Interscience Publishers, John Wiley & Sons)
- . 2006, Physics of Fully Ionized Gases, 2nd edn. (Mineola, New York: Dover Publications, Inc.)
- Spruit, H. 1982, Solar Phys., 75, 3
- . 2012, Progr. Theor. Physics Supplement, 195, 185
- Spruit, H., & Roberts, B. 1983, Nature, 304, 401
- Spruit, H., & Van Ballegooijen, A. 1982, Astron. Astrophys., 106, 58, erratum 113 (1982) 350
- Srednicki, M. 1985, Nuclear Physics, B260, 689
- Stein, R. F. 2012, Living Reviews in Solar Physics, 9, doi:10.12942/lrsp-2012-4
- Steinfadt, J. D. R., Bildsten, L., & Arras, P. 2010, The Astrophysical Journal, 718, 441
- Sterling, A. C., Moore, R. L., Falconer, D. A., & Adams, M. 2015, Nature, 523, 437
- Stix, M. 2004, The Sun: An Introduction (Berlin: Springer)
- Sturrock, P. A., Weber, M., Wheatland, M. S., & Wolfson, R. 2001, The Astrophysical Journal, 548, 492
- Turner, M. S. 1990, Physics Reports (Review Section of Physics Letters), 197, 67
- Uchaikin, V. V. 2013, Physics-Uspekhi, 56, 1074
- Valyavin, G., Antonyuk, K., Plachinda, S., et al. 2011, The Astrophysical Journal, 734, 17
- Valyavin, G., Shulyak, D., Wade, G. A., et al. 2014, Nature, 515, 88
- van Horn, H. M. 1979, Physics Today, 32, 23
- Vysotskii, M. I., Zel’dovich, Y. B., Khlopov, M. Y., & Chechetkin, V. M. 1978, JETP letters, 27, 533
- Winget, D. E., & Kepler, S. O. 2008, ARA&A, 46, 157
- Winterberg, F. 2015, [arXiv:1503.03003 \[physics.gen-ph\]](#)
- Wuensch, W. U., Panfilis-Wuensch, S. D., Semertzidis, Y. K., et al. 1989, Phys. Rev. D, 40, 3153

- Zhang, J., Zhang, B., Li, T., et al. 2015, The Astrophysical Journal Letters, 799, L27
- Zhitnisky, A. P. 1980, Sov. J. Nucl. Phys., 31, 260
- Zioutas, K., Tsagri, M., Semertzidis, Y., et al. 2009, New J. Physics, 11, 105020, [arXiv:0903.1807](#)
[\[astro-ph.SR\]](#)
- Zioutas, K., Tsargi, M., Semertzidis, Y., et al. 2007, [arXiv:astro-ph/0701627](#)
- Zwaan, C. 1978, Solar Phys., 60, 213